Received: 29 December 2023 | Revised: 27 July 2024 | Accepted: 29 September 2024

DOI: 10.1002/jev2.70002

RESEARCH ARTICLE

A switch from lysosomal degradation to secretory autophagy initiates osteogenic bone metastasis in prostate cancer

Xiaoyu Wei[1] | **Mengmeng Liang**[1,2] | **Min Deng**[3] | **Ji Zheng**[3] | **Fei Luo**[1] | **Qinyu Ma**[1,4,5,6]

[1]Department of Orthopedics, Southwest Hospital, Third Military Medical University, Chongqing, China

[2]Institute of Environment and Operational Medicine, Academy of Military Medicine Sciences, Academy of Military Sciences, Tianjin, China

[3]Department of Urology, Xinqiao Hospital, Third Military Medical University, Chongqing, China

[4]Institute of Cancer, Xinqiao Hospital, Third Military Medical University, Chongqing, China

[5]Chongqing Key Laboratory of Immunotherapy, Chongqing, China

[6]Shigatse Branch, Xinqiao Hospital, Third Military Medical University, Shigatse, China

Correspondence
Fei Luo, Department of Orthopedics, Southwest Hospital, Third Military Medical University, Gaotanyan Street No. 30, Chongqing 400038, China. Email: luofeispine@126.com

Qinyu Ma, Department of Orthopedics, Southwest Hospital, Third Military Medical University, Gaotanyan Street No. 30, Chongqing 400038, China. Email: maqinyu@tmmu.edu.cn

Funding information
National Natural Science Foundation of China, Grant/Award Numbers: 82202710, 82302747

Abstract

The identification of both autophagy-related material degradation and unconventional secretion has paved the way for significant breakthroughs linking autophagy to a plethora of physiological processes and disease conditions. However, the mechanisms that coordinate these two pathways remain elusive. Here, we demonstrate that a switch from the lysosomal degradation to a secretory autophagy pathway is governed by protein tyrosine phosphatase 1B (PTP1B, encoded by *PTPN1*). Dephosphorylation at two tyrosine residues of syntaxin17 (STX17) by PTP1B reduces autophagosome-lysosome fusion while switching the cells to a secretory autophagy pathway. Both PTP1B overexpression and tumour-derived extracellular vesicles (EVs) can activate the secretory autophagy pathway in osteoblasts. Moreover, we demonstrate that osteoblastic LC3+ EVs, generated via the secretory autophagy pathway, are the primary contributor to tumour-associated bone remodelling in prostate cancer. Depletion of tumour-derived EVs secretion or genetic ablation of osteoblastic PTP1B rescues aberrant bone remodelling and lesions, highlighting the relevance between LC3+ EVs and the formation of bone metastatic niche. Our results reveal the significance of tumour-regulated PTP1B in the fate decision of autophagosomes, and propose a role ofLC3+ EVs in shaping the bone metastatic niche.

KEYWORDS
autophagosome-lysosome fusion, bone metastatic niche, extracellular vesicles, secretory autophagy, tumour-associated bone remodelling

1 | INTRODUCTION

Autophagosomes play a crucial role in the process of autophagy, whereby they undergo trafficking and fusion with acidified lysosomal compartments to form autolysosomes, which are specialized organelles that facilitate efficient cargo degradation and maintenance of intracellular proteostasis. Specific membrane fusion between intracellular vesicles is generally coordinated by SNARE complexes. A SNARE complex consists of an autophagosome-localized Q-SNARE STX17, SNAP29, and a lysosome-localized R-SNARE VAMP8, identified as the core machinery responsible for the autophagosome-lysosome fusion process (Itakura et al., 2012). Additionally, recent studies have revealed the involvement of YKT6, an R-SNARE protein, in the fusion process between autophagosomes and lysosomes (Matsui et al., 2018).

Xiaoyu Wei and Mengmeng Liang contributed equally to this work.

Although autophagy is commonly perceived as a lysosomal degradation process, genetic evidence suggests that autophagy pathway components (ATGs) also govern the release of inflammatory cytokines (Cadwell & Debnath, 2018; Dupont et al., 2011), extracellular vesicle (EV) production (Keller et al., 2020; Leidal et al., 2020), extracellular release of pathogens (Li et al., 2020; van der Grein et al., 2022), lysozyme (Bel et al., 2017), secretory lysosomes (DeSelm et al., 2011), and unconventional secretion of proteins lacking an N-terminal signal sequence (Dupont et al., 2011; Malhotra, 2013). Collectively termed as 'secretory autophagy', these processes involve autophagosomes releasing their contents into the extracellular space without fusing with lysosomes, occurring both under normal conditions and during disease (Cadwell & Debnath, 2018). Recent studies raise that secretory autophagy relies on the LC3-conjugation machinery to control the selective loading of specific proteins into EVs (Leidal et al., 2020) and function as an alternate route to maintain intracellular proteostasis in response to inhibition of lysosomal degradation (Solvik et al., 2022). However, current understanding of secretory autophagy is still limited. First, the activation requirements of the secretory autophagy pathway and its relationship with lysosomal degradation remain unclear. Second, the effects of the secretory autophagy pathway on cells themselves and the underlying biological functions of its products on surrounding cells are not well elucidated.

Bone is the primary site of metastasis for prostate cancer. The imbalance between bone formation and resorption in the bone microenvironment, resulting from tumour growth, results in the development of bone metastatic lesions exhibiting either an osteogenic or osteolytic phenotype (Glass et al., 2005; Kim et al., 2020). In bone metastatic niches, tumour cells interact with diverse populations of bone marrow resident cells, including osteoblasts and osteoclasts (Nguyen et al., 2009). We previously observed a distinct disparity in the cargo composition of EVs released from PC3, which induced an osteolytic phenotype, compared to C4-2 that induced an osteogenic phenotype (Ma et al., 2021). Expanding upon this finding, we further elucidated the underlying mechanism by which PC3 EVs promoted the osteolytic phenotype (Ma et al., 2021).

Here, we describe a switch from the lysosomal degradation to the secretory autophagy pathway mediated by PTP1B-STX17 axis. Additionally, we investigate the correlation between osteoblast-derived LC3+ EVs via the secretory autophagy pathway and osteogenic destruction in the bone metastatic niche of prostate cancer.

2 | RESULT

2.1 | PTPN1 knockout mediates autophagosome maturation into autolysosome independent of lysosome acidification

Previous studies have linked the gene expression level of *PTPN1* with endoplasmic reticulum stress and autophagy (Barahona et al., 2022; Solvik et al., 2022), yet the precise underlying mechanism remains elusive. To investigate further, we first conducted a comprehensive analysis in HEK293T cells with knockout of *PTPN1* using Cas9/single-guide RNAs (sgRNAs) system (Figure S1a,b). The fact that PTP1B is colocalized with LC3 suggests a potential connection between PTP1B and autophagy (Figure S1c). To further elucidate the role of *PTPN1* in autophagic degradation, we transfected cells with a mCherry-EGFP-LC3 vector, which enables discrimination between autophagosomes and autolysosomes based on the differential acid stability of GFP and mCherry (van der Grein et al., 2022). As expected, the yellow puncta were increased while the red puncta did not significantly change upon treatment with lysosomal inhibitor Bafilomycin A1 (BafA1) compared to DMSO group, indicating that autophagosome maturation into autolysosome is blocked (Figure S1d–f). In contrast, both yellow and red puncta were increased upon Rapamycin treatment, suggesting activation of autophagic flux and autolysosome formation (Figure S1d–f). Notably, sg*PTPN1* reduced the number of green puncta compared to sgSRC, while the red puncta remained unchanged (Figures 1a and S1g). Furthermore, *PTPN1* knockout increased the colocalization of autophagosome marker LC3B and LAMP1-positive vesicles both in the presence and absence of Torin1 (Figure 1b). Importantly, sg*PTPN1* cells treated with BafA1 exhibited a larger autolysosome size with significantly increased numbers of ILVs in the autolysosome lumen (Figure 1c,d). These data suggest that *PTPN1* knockout enhances fusion between autophagosomes and lysosomes. We further confirmed whether the induction of autolysosomes upon *PTPN1* knockout was attributed to alterations in lysosomal activity. We observed a reduction in lysosomal activity in cells treated with acidification inhibitor BafA1 and chloroquine (Figure S1h,i). Unexpectedly, no significant differences were observed in the average Lysosensor signal, lysosomal pH, or ACP2 acid phosphatase activity between sg*PTPN1* cells and sgSRC cells (Figure 1e,f). Similarly, *PTPN1* depletion did not affect the protein expression of LAMP1 (Figure S1j). These data indicate that *PTPN1* knockout does not affect lysosomal acidification. Together, our results suggest that *PTPN1* knockout mediates autophagosome maturation into autolysosome in a manner independent of lysosomal acidification.

2.2 | PTP1B dephosphorylates STX17 at Tyr157 and Tyr227

Given that both lysosome acidification and autophagosome-lysosome fusion can independently promote autophagosome maturation (Mauvezin & Neufeld, 2015), and that *PTPN1* knockout does not affect lysosome acidification, we further investigated

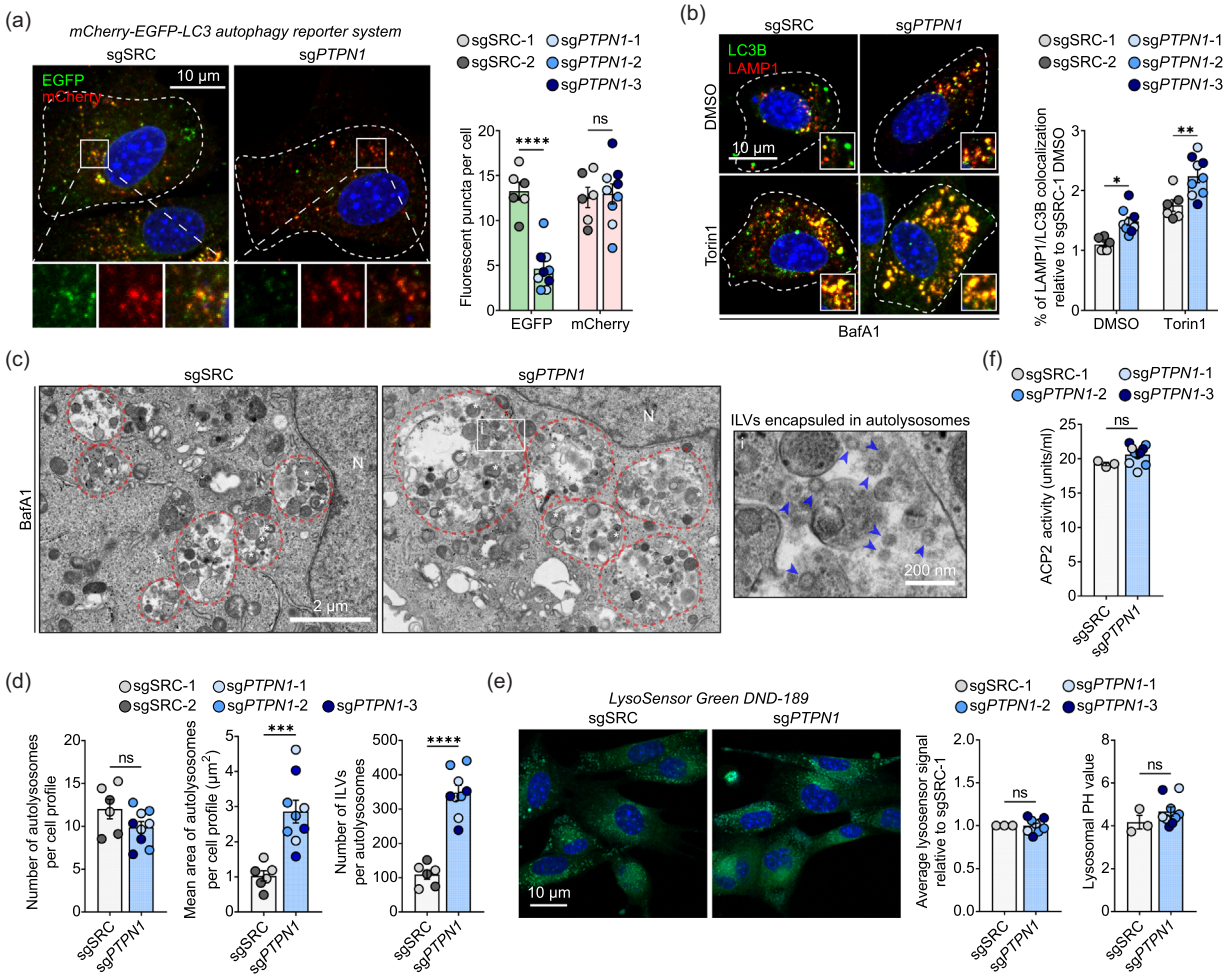

FIGURE 1 *PTPN1* knockout mediates autophagosome maturation into autolysosome independent of lysosome acidification. **(a)** Left, sgSRC and sg*PTPN1* cells transfected with mCherry-EGFP-LC3 reporter plasmid were imaged for EGFP and mCherry fluorescence using confocal microscopy. Cell borders are delineated by white dashed lines. Scale bars, 10 μm. Right, quantification of EGFP and mCherry positive fluorescent puncta per individual cell. $n = 6$ (sgSRC) or 9 (sg*PTPN1*) biological replicates. Each dot indicates a mean value from 3 to 5 individual cells. **(b)** Left, representative immunofluorescence staining of LC3B and LAMP1 in sgSRC and sg*PTPN1* cells. Cells were treated for 2 h with BafA1 (100 nM), and where indicated, Torin1 (250 nM) was added for 6 h. Cell borders are delineated by white dashed lines. Scale bars, 10 μm. Right, Quantification shows the percentage (%) of colocalization of LC3B and LAMP1 relative to sgSRC-1 cells treated with DMSO vehicle. $n = 6$ (sgSRC) or 9 (sg*PTPN1*) biological replicates. Each dot indicates a mean value from 3 to 5 individual cells. **(c)** Left and middle, representative TEM images of sgSRC and sg*PTPN1* cells treated for 2 h with BafA1 (100 nM). Autolysosomes are indicated by red dashed lines. Asterisks label autophagic cargos inside autolysosomes. N, nucleus. Right, examples of ILVs encapsuled in autolysosomes (corresponding to i from the middle image). Blue arrows indicate individual ILVs. Scale bars, 2 μm (left and middle); 200 nm (right). **(d)** Quantification shows the number of autolysosomes per cell profile, the mean area of individual autolysosomes, and the number of ILVs inside autolysosomes. $n = 6$ (sgSRC) or 9 (sg*PTPN1*) biological replicates. Each dot indicates a mean value from 3 to 5 individual cells. **(e)** Quantitative comparison of lysosomal function between sgSRC and sg*PTPN1* cells. Bar graphs display the average Lysosensor staining intensity (**left**) and lysosomal PH value (**right**) relative to sgSRC-1 cells. $n = 3$ (sgSRC) or 9 (sg*PTPN1*) biological replicates. Each dot indicates a mean value from 3 to 5 individual cells. **(f)** Quantitative comparison of ACP2 activity between sgSRC and sgPTPN1 cells. $n = 3$ (sgSRC) or 9 (sg*PTPN1*) biological replicates. **(a,b,d,e,f)** Data are presented as mean values ± s.e.m.; multiple unpaired *t*-tests **(a,b)**; two-sided unpaired *t*-tests **(d,e,f)**. $^{****}p < 0.0001$, $^{***}p < 0.0005$, $^{**}p < 0.005$, and $^{*}p < 0.05$.

whether *PTPN1* promotes autophagosome maturation by inducing autophagosome-lysosome fusion. Cargo sorting, intracellular fusion, and extracellular release of vesicles are primarily coordinated by several proteins located on the vesicle surface (Kalluri & LeBleu, 2020; Nakatogawa, 2020). Therefore, we hypothesized that PTP1B may modulate autophagosome-lysosome fusion through protein-protein interactions. Using the AlphaFold2 deep learning algorithm, we analysed the protein-level interaction of PTP1B with SNARE proteins that initiate vesicle fusion and autophagy receptors that mediate cargo selection of autophagosomes. Among all predicted candidates, three Q-SNAREs including STX7, STX17, SNAP29, and one R-SNARE YKT6 exhibited acceptable predicted binding scores with PTP1B (predicted DockQ > 0.23) (Figure 2a), along with a greater number of hydrogen and ionic bonds (predicted polar contacts > 5) (Fig. S2). We subsequently confirmed distinct degrees of cytoplasmic colocalization between these proteins and PTP1B, with the average colocalization intensity of STX17 and PTP1B approaching 60% (Figure 2b,c). Furthermore, the interaction between endogenous PTP1B and STX17 was then corroborated by using a coimmuno-

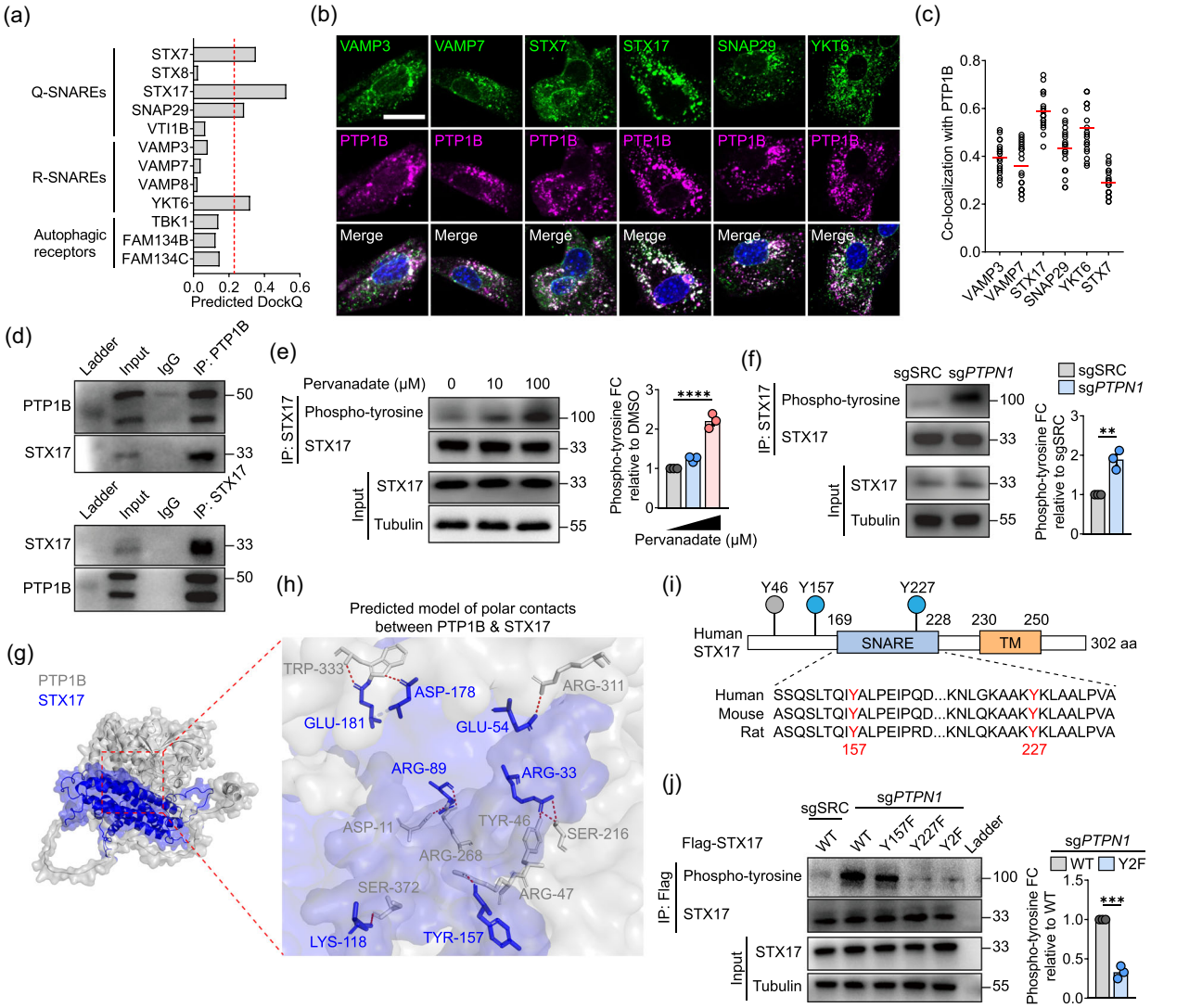

FIGURE 2 PTP1B dephosphorylates STX17 at Tyr157 and Tyr227. **(a)** Predicted DockQ scores for each protein involved in the interaction with PTP1B. The predicted DockQ ≥ 0.23 represents an acceptable binding possibility between proteins is indicated by a red dashed line. **(b)** Representative immunofluorescence staining of PTP1B and 3 Q-SNAREs or 3 R-SNAREs in cells. Scale bars, 10 μm. **(c)** Colocalization between PTP1B and the indicated SNARE proteins (green puncta) was quantified in $n = 20$ cells as in **(b)**. Data are presented as Pearson's correlation coefficient (r). **(d)** Co-immunoprecipitation assay using PTP1B and STX17 as bait protein, respectively, demonstrated the interaction between PTP1B and STX17 with IgG as a negative control. Representative western blot images from three independent experiments are shown. **(e)** Left, Western blot analysis showing immunoprecipitation experiment of cells treated with indicated concentration of pervanadate for 15 min. Right, quantitative analysis of phospho-tyrosine fold change relative to DMSO. $n = 3$ biological replicates. **(f)** Left, western blot analysis showing immunoprecipitation experiment of sgSRC and sg*PTPN1* cells. Right, quantitative analysis of phospho-tyrosine fold change relative to sgSRC. $n = 3$ biological replicates. **(g,h)** Predicted three-dimensional heterodimer model of the PTP1B/STX17 complex. The overview of binding region between full-length PTP1B and STX17 is indicated by a red dashed line in **(g)** and 10 residue-residue interactions with polar contacts within 3 Åm depicted in **(h)**. **(i)** Top, schematic presentation of the domain structures of human STX17. The phosphorylation modification of two out of the three tyrosine residues, namely, Y157 and Y227, has been previously reported. Bottom, an amino acid sequence alignment of the SNARE domain of STX17 in three species, the conserved tyrosine residues are highlighted in red font. **(j)** Left, sg*PTPN1* cells transfected with WT, Y157F, Y227F and Y2F mutants of STX17 were immunoprecipitated with anti-FLAG antibody and subjected to western blot analysis. Right, bar graph shows quantification of phospho-tyrosine levels of Y2F mutation relative to WT. $n = 3$ biological replicates. **(e,f,j)** Data are presented as mean values ± s.e.m.; one-way ANOVA with Dunnett's multiple comparisons test **(e)**; two-sided unpaired *t*-tests **(f,j)**. $^{****}p < 0.0001$, $^{***}p < 0.0005$, and $^{**}p < 0.005$.

precipitation assay (Figure 2d). STX17, located on the surface of completed autophagosomes, is one of the most crucial Q-SNAREs that binds to SNAP29 and VAMP8 to form a SNARE complex for mediating autophagosome-lysosome fusion (Itakura et al., 2012). Of note, we observed an increase in the phospho-tyrosine level of STX17 in cells treated with the tyrosine phosphatase inhibitor pervanadate and those with *PTPN1* knockout (Figure 2e,f), indicating a reduction in tyrosine dephosphorylation of STX17 upon *PTPN1* knockout.

To further confirm the specific residue sites involved in protein interaction, we investigated the binding mechanism between PTP1B and STX17. We used AlphaFold-Multimer to generate a heterodimer model between full-length PTP1B and STX17

(Figure 2g and Table S3). The interprotein polar contacts that stabilize the heterodimer structure were identified by molecular docking simulations and molecular dynamics calculations (Figure 2h). These methods exhibit high precision and dependability when investigating molecular binding systems (Jumper et al., 2021). The results showed that seven residues of STX17, including tyrosine-157 residue (Y157), engage in polar contacts with PTP1B (Figure 2h). Indeed, we examined all three tyrosine residues of STX17 using PhosphoSitePlus and identified two unique sites, Y157 and Y227, that are likely to undergo dynamic phosphorylation and dephosphorylation events (Figure 2i). To experimentally demonstrate the functional role of STX17 phosphorylation, we generated separate phenylalanine mutations at Y157 and Y227 (phosphomutant Y157F and Y227F) or a combined mutation (phosphomutant Y2F). Consistent with silico analysis, co-immunoprecipitation experiments revealed that compared to wild-type, phosphomutant Y2F almost completely diminished the tyrosine phosphorylation of STX17 in *PTPN1* knockout cells (Figure 2j). These findings suggest that PTP1B targets and dephosphorylates Q-SNARE STX17 at Tyr157 and Tyr227 residues.

2.3 | STX17 dephosphorylation negatively regulates SNARE complex formation and autophagosome-lysosome fusion

To further elucidate the regulatory role of PTP1B in autophagosome-lysosome fusion via STX17 dephosphorylation at Tyr157 and Tyr227 residues, we simultaneously mutagenized Tyr157 and Tyr227 of STX17 into glutamic acids (phosphomimetic Y2E) in sg*PTPN1* cells, and assessed its impact on autophagosome maturation. Interestingly, Torin1 stimulation led to a decrease in the colocalization of LC3B and LAMP1-positive vesicles in STX17-Y2F cells (Figure S3a,b), while LC3B was significantly more colocalized with LAMP1-positive vesicles even without Torin1 treatment in STX17-Y2E cells (Figure S3a, b). At the phenotypic level of autolysosomes, STX17-Y2F mutation resulted in a significant reduction in both the size of autolysosomes and the number of ILVs within autolysosomes (Figure 3a,b). In contrast, although STX17-Y2E did not further increase the size of autolysosomes, it moderately increased the number of ILVs within them (Figure 3a,b). These data suggest that STX17 dephosphorylation by PTP1B reduces autophagosome-lysosome fusion.

We then investigated whether dephosphorylation of STX17 by PTP1B regulated the formation of STX17-SNAP29-VAMP8 SNARE complex. Ectopic expression of Flag-STX17 in sg*PTPN1* cells significantly increased binding efficiency with VAMP8 and SNAP29 compared to sgSRC control cells (Figure 3c,d). Notably, transfection of Flag-STX17-Y2E mutant enhanced Flag binding efficiency with VAMP8 and SNAP29 in sg*PTPN1* cells, while Flag-STX17-Y2F completely abolished the binding of Flag to SNAP29 and VAMP8 (Figure 3e,f). Together, these data suggest that dephosphorylation of STX17 by PTP1B impedes the formation of STX17-SNAP29-VAMP8 SNARE complex and autophagosome-lysosome fusion.

2.4 | PTP1B determines the switch from lysosomal degradation to the secretory autophagy pathway

Unconventional secretion via EV release provides an alternative pathway for clearing sequestered material and maintaining proteostasis during lysosomal inhibition (Solvik et al., 2022). We wondered if autophagosome-lysosome fusion regulated by PTP1B is also implicated in autophagosome content release. To this end, we initially investigated the secretory autophagy phenotype upon PTP1B knockout. However, no discernible alteration was observed in either the protein content of cell lysate and EV fraction or the EV yield between sg*PTPN1* cells and sgSRC cells (Figure S4a). In both groups, the proportion of LC3+ EVs was only approximately 1% of the total EV population. Additionally, all released LC3 components released by cells were susceptible to protease K treatment, indicating that these free LC3 proteins were not incorporated into EVs (Figure S4b–d). These findings suggest that secretory autophagy is not a constitutive physiological process and that reducing PTP1B levels does not further impede the release of autophagy-associated vesicles.

Therefore, we established a cell model with PTP1B overexpression in HEK293T cells (Figure S4e,f). The lysosomal pH value showed no statistical difference between PTP1B-overexpressing cells and the empty control (Figure S4g), consistent with the observations that PTP1B does not impact lysosomal acidification. We observed that PTP1B overexpression led to an increase in both the protein content of EV fraction and EV yield, while having no impact on the protein content of cell lysatecompared to empty vector-transfected cells (Figure 4a). While a portion of LC3 protein released by PTP1B-overexpressing cells remained susceptible to proteinase K treatment, another fraction of LC3 signal was protected from protease digestion in the absence of detergent, indicating that this fraction of protected LC3 is enclosed within the EV lumen (Figure 4b,c). Importantly, the percentage of LC3+ EV was significantly higher in the PTP1B-overexpressing cells (24.35 ± 0.46%) compared to that in the empty control cells (1.24 ± 0.31%) (Figure 4d). We further investigated whether PTP1B overexpression promotes secretory autophagy through STX17 dephosphorylation. The STX17-Y2E mutation in PTP1B-overexpressing cells significantly attenuated the secretory autophagy phenotype, as evidenced by reduced protein content of EV fraction, decreased EV yield and lower LC3+ EV proportion (Figure 4e). These data suggest that dephosphorylation of STX17 by PTP1B functions as an activator for the secretory autophagy pathway. Notably, at the phenotypic level, the size and quantity of autolysosomes, as well as the number of ILVs within

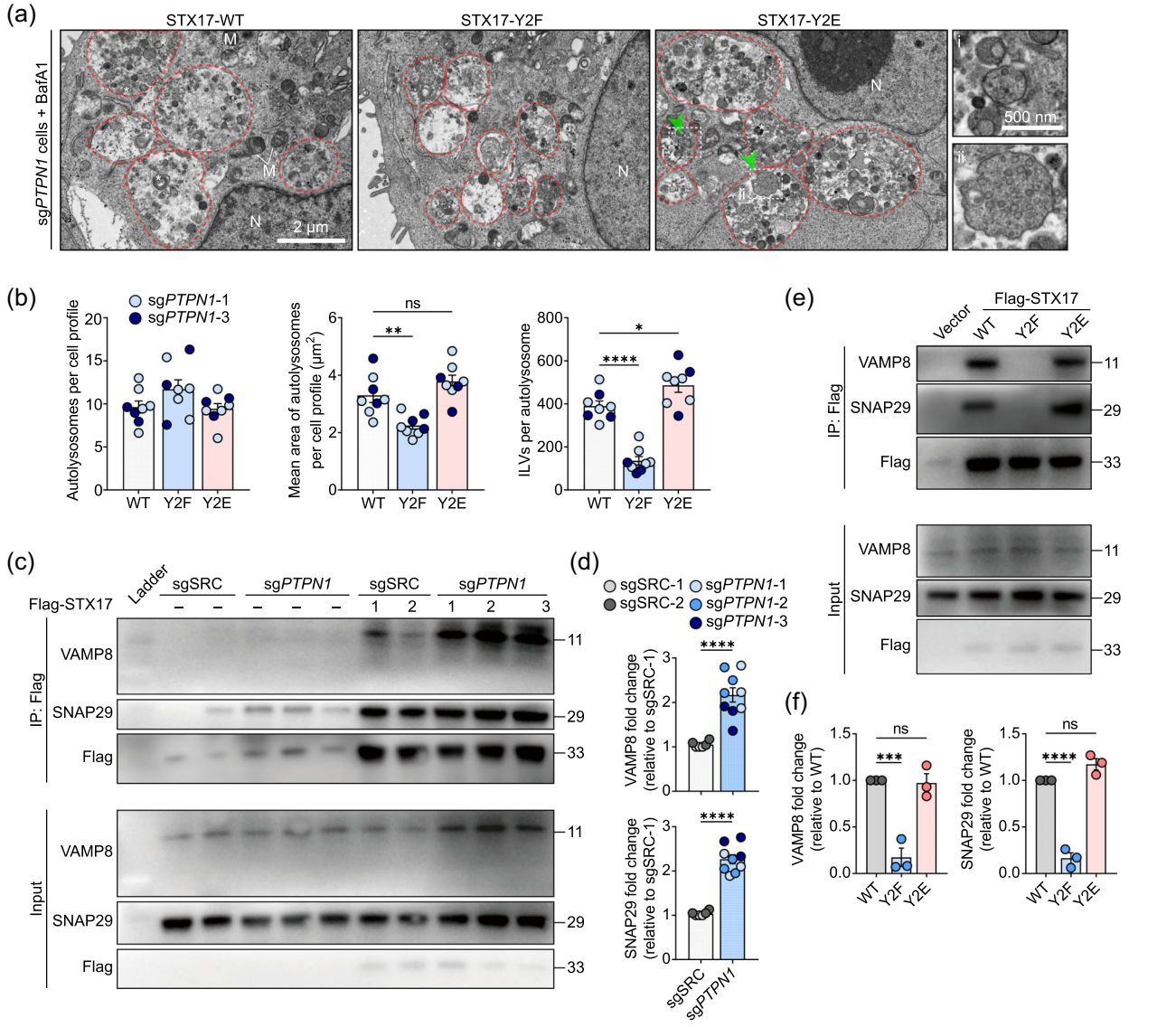

FIGURE 3 STX17 dephosphorylation negatively regulates SNARE complex formation and autophagosome-lysosome fusion. **(a)** Representative TEM images of sg*PTPN1* cells transfected with STX17-WT, STX17-Y2F, and STX17-Y2E mutants. Cells were treated for 2 h with BafA1 (100 nM). Y2F: The tyrosine residues in STX17 were substituted with phenylalanines rendering them non-phosphorylatable. Y2E: The tyrosine residues were substituted with glutamic acids, leading to a sustained phosphorylation. Autolysosomes are indicated by red dashed lines. Asterisks label autophagic cargos inside autolysosomes. Green arrows indicate MVBs inside autolysosomes (corresponding to i and ii at the right panel). N, nucleus. M, mitochondrion. Scale bars, 2 μm (left); 500 nm (right). **(b)** Quantification shows the number of autolysosomes per cell profile, the mean area of individual autolysosomes, and the number of ILVs inside autolysosomes. Enlarged autolysosomes and a higher abundance of ILVs inside autolysosomes were demonstrated in Y2F cells. $n = 8$ biological replicates. Each dot indicates a mean value from 3 to 5 individual cells. **(c)** Lysate from the cell cultures of sgSRC and sg*PTPN1* were immunoprecipitated with anti-FLAG antibody and subjected to western blot analysis. **(d)** Bar graphs show quantification of VAMP8 and SNAP29 fold change in sg*PTPN1* cells relative to sgSRC-1 cells. $n = 6$ (sgSRC) or 9 (sg*PTPN1*) biological replicates. **(e)** Lysate from the cell cultures of sg*PTPN1* cells transfected with STX17-WT, STX17-Y2F, and STX17-Y2E mutants were immunoprecipitated with anti-FLAG antibody and subjected to western blot analysis. **(f)** Bar graphs show quantification of VAMP8 and SNAP29 fold change in STX17-Y2F and STX17-Y2E relative to STX17-WT. $n = 3$ biological replicates. **(b,d,f)** Data are presented as mean values ± s.e.m.; one-way ANOVA with Dunnett's multiple comparisons tests **(b,f)**; two-sided unpaired *t*-test **(d)**. $^{****}p < 0.0001$, $^{***}p < 0.0005$, $^{**}p < 0.005$ and $^{*}p < 0.05$.

autolysosomes were significantly reduced in PTP1B-overexpressing cells treated with BafA1 (Figure 4f,g). Conversely, in PTP1B-overexpressing cells treated with BafA1, STX17-Y2E mutation markedly increased the size and number of autolysosomes along with ILV abundance, as compared to STX-WT control (Figure 4h,i). These data suggest that elevated levels of PTP1B govern the transition from autolysosomal degradation to secretory autophagy pathway.

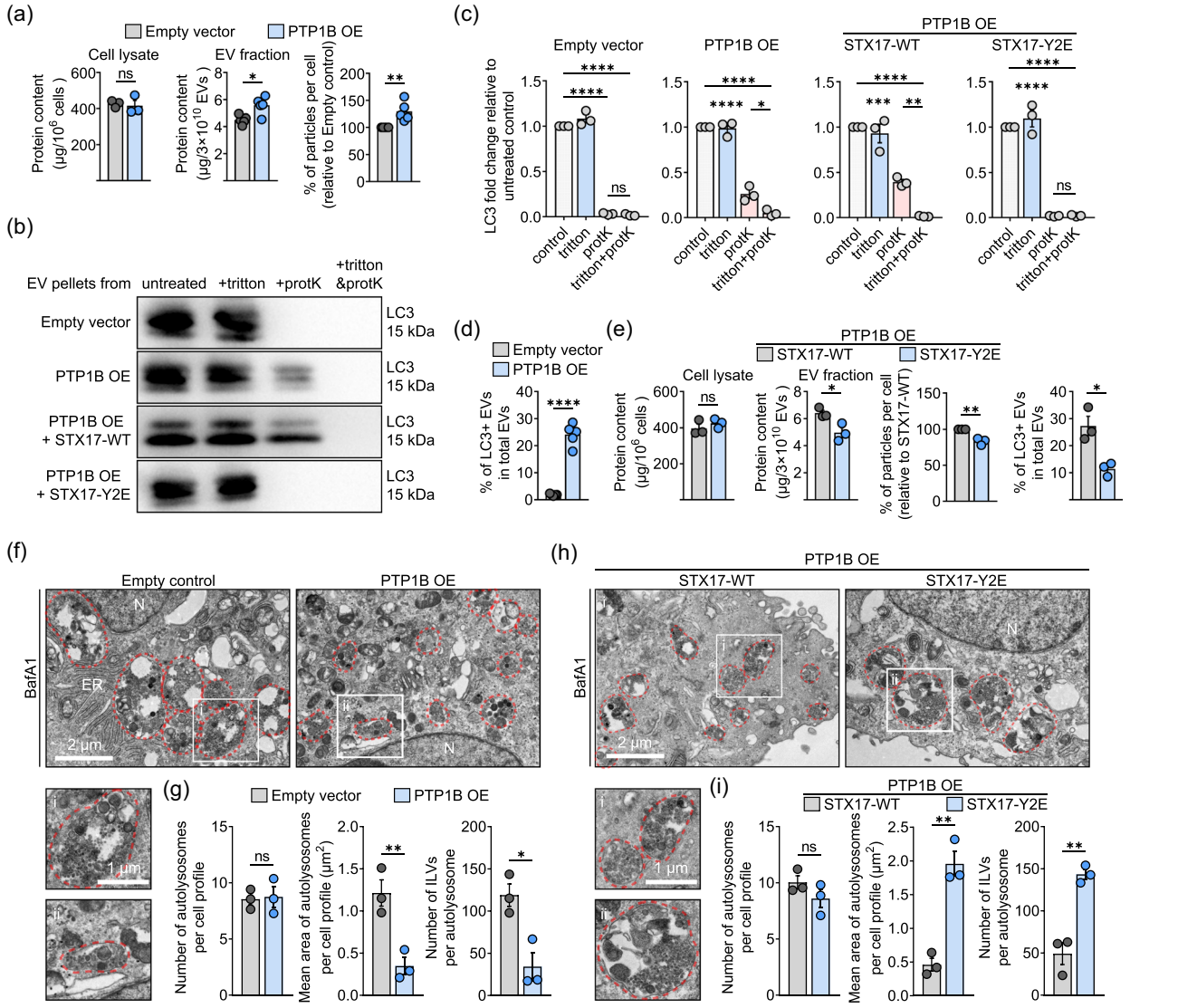

FIGURE 4 PTP1B determines the switch from lysosomal degradation to the secretory autophagy pathway. **(a)** Left and middle, quantitative protein content of both the cell lysate and EV fraction from PTP1B OE cells was determined using the BCA assay. Right, quantification shows concentration of particles from individual PTP1B OE cells relative to empty vector-transfected cells. $n = 3$ (left) and 5 (middle and right) biological replicates. **(b)** EV pallets from indicated cells were treated with proteinase K in the absence or presence of 0.2% triton. Depicted are representative blots for the presence of LC3. **(c)** Quantitative analysis of LC3 fold change relative to untreated control of samples in (b). $n = 3$ biological replicates. **(d)** The percentage (%) of LC3+ EV proportion in total EVs extracted from empty control and PTP1B OE cells was determined using NTA and flowcytometry. $n = 5$ biological replicates. **(e)** Left and middle left, quantitative protein content of both the cell lysate and EV fraction from PTP1B OE cells transfected with STX17-WT and STX17-Y2E mutants. Middle right, quantification shows the concentration of particles from STX17-Y2E cells relative to cells transfected with STX17-WT. Right, the percentage (%) of LC3+ EV proportion in total EVs from STX17-WT and STX17-Y2E cells. $n = 3$ biological replicates. **(f)** Top, representative TEM images of PTP1B OE cells and empty vector control cells. Cells were treated for 2 h with BafA1 (100 nM). Autolysosomes are indicated by red dashed lines. N, nucleus. ER, endoplasmic reticulum. Bottom left, examples of individual autolysosomes are depicted (corresponding to i and ii from the top image). Scale bars, 2 µm (top); 1 µm (bottom left). **(g)** Quantification shows the number of autolysosomes per cell profile, the mean area of individual autolysosomes, and the number of ILVs inside autolysosomes in PTP1B OE cells and empty vector control cells. $n = 3$ biological replicates. Each dot indicates a mean value from 3 to 5 individual cells. **(h)** Top, representative TEM images of PTP1B OE cells transfected with STX17-WT and STX17-Y2E mutants. Cells were treated for 2 h with BafA1 (100 nM). Autolysosomes are indicated by red dashed lines. N, nucleus. Bottom left, examples of individual autolysosomes are depicted (corresponding to i and ii from the top image). Scale bars, 2 µm (top); 1 µm (bottom left). **(i)** Quantification shows the number of autolysosomes per cell profile, the mean area of individual autolysosomes, and the number of ILVs inside autolysosomes in PTP1B OE cells transfected with STX17-WT and STX17-Y2E mutants. $n = 3$ biological replicates. Each dot indicates a mean value from 3 to 5 individual cells. **(a,c,d,e,g,i)** Data are presented as mean values ± s.e.m.; one-way ANOVA with Tukey's post hoc test for multiple comparisons **(c)**; two-sided unpaired *t*-tests **(a,d,e,g,i)**. $^{****}p < 0.0001$, $^{***}p < 0.0005$, $^{**}p < 0.005$ and $^{*}p < 0.05$.

2.5 | Osteoblastic LC3+ EVs from secretory autophagy pathway initiate early mineralization

Previous studies have suggested a close association between autophagy and mineralization in both osteoblasts (Yoshida et al., 2022) and osteocytes (Vrahnas et al., 2019). However, the role of secretory autophagy in this process remains unclear. To further investigate the impact of secretory autophagy on osteogenic differentiation and mineralization, we established a model wherein PTP1B was overexpressed in the osteogenic precursor cell line MC3T3-E1 (Figure S5a,b). We observed an increase in autophagic activity, as well as a higher number of MVBs and amphisomes containing both ILVs and autophagosomes in MC3T3-E1 overexpressing PTP1B (Figure 5a,b). Furthermore, compared to empty control, PTP1B overexpression resulted in a significant increase in both protein content and yield of EVs (Figures 5c and S5c). Notably, we found that the content of LC3 protein in the EV fraction of PTP1B-overexpressing cells was higher than that of the control, while the expression of TSG101 and CD81 in these two groups was similar (Figure 5d). The percentage of LC3-positive EVs in MC3T3-E1 cells transfected with empty vectors was only 1.98%, whereas overexpression of PTP1B significantly increased the proportion to 58.28% (Figure S5d). These data demonstrate that PTP1B overexpression effectively triggers secretory autophagy in MC3T3-E1 cells.

We subsequently purified EVs and directly compared the osteogenic capacity of LC3+ EVs with that of control EVs. The results showed that alkaline phosphatase (ALP) activity in LC3+ EVs (13.24 ± 0.69) was approximately four times higher than that in control EVs (3.15 ± 0.15) when equal amounts of EVs were compared (Figure 5e), suggesting the mineralization potential of LC3+ EVs. We mixed LC3+ EVs with control EVs in varying ratios and investigated the impact of the mixed EV populations on mineralization. As expected, the augmented proportion of LC3+ EVs demonstrated a positive correlation with the degree of collagen matrix-mediated mineralization and the expression levels of osteogenic markers (Figures 5f,g and S5e). These data support the notion that osteoblastic LC3+ EVs generated through PTP1B-mediated secretory autophagy pathway possess the ability to initiate mineralization.

2.6 | Presence of LC3+ EVs in the osteogenic bone metastatic niche

We and others have previously proposed that intercellular communication between tumour cells and bone-resident cells within the bone metastatic niche generates phenotypic variations in tumour-associated bone remodelling (Croucher et al., 2016), such as the transmission of osteolytic signals from tumours to promote osteoclastogenesis and mediate osteolytic destruction (Ma et al., 2021). We hypothesized that osteoblastic LC3+ EVs derived from the secretory autophagy pathway may contribute to tumour-induced bone remodelling. We previously identified two tumour cell lines with opposite phenotypes of bone remodelling, the osteolytic phenotype-inducing cell line PC3 and the osteogenic phenotype-inducing cell line C4-2 (Ma et al., 2021). We orthotopically established a cell line-derived xenograft animal model, by injecting PC3 and C4-2 into the tibial medullary cavity of BALB/c nude mice. This model enables the evaluation of the interplay between bone-resident cells and colonized tumour cells in the bone marrow niche (Berish et al., 2018). We monitored the growth of tumour cells stably expressing the firefly luciferase reporter by performing bioluminescence imaging (BLI) weekly. Although no difference was observed in engraftment rate between the two cell lines (Figure 5h), PC3 induced a stronger tumour burden by week 5 while C4-2 essentially stopped growing from week 4 (Figure 5i). Von Kossa staining of undecalcified tumour slices confirmed that the mineralized tissues in C4-2, but not in PC3, were composed of bone matrix and surrounded by osteoblast-like cells or osteoids (Figure 5j,k), indicating an osteogenic property of the C4-2 bone metastatic niche. Corroborative evidence for this also came from increased expression of osteogenic markers *OSX*, *RUNX2* in C4-2 tumours (Figure 5l). While the xenograft lysates of either C4-2 or PC3 contained more EVs as compared with normal bone marrow (Figure 5m), the LC3+ EV proportion in C4-2 xenografts was significantly higher than that in either bone marrow or PC3 (Figure 5 m). These results indicated a specific presence of LC3+ EVs in the osteogenic bone metastatic niche.

2.7 | Tumoral EVs induce LC3+ EV generation from osteoblasts

We further investigated the mechanism of LC3+ EV generation in osteogenic C4-2 tumours. CM from neither osteoclasts nor osteoblasts affected the LC3+ EV proportion from C4-2 (Figure S6a). However, CM from C4-2 induced secretory autophagy of MC3T3-E1 cells characterized by increased protein content of EV fraction, EV yield and LC3+ EV proportion (Figure S6b–d), and upregulated gene expression of both osteogenic markers and *PTPN1* (Figure S6e). Importantly, depletion of EVs in CM markedly impaired the capacity of CM to induce secretory autophagy and mineralization (Figures 6a,b and S6f,g), indicating that EVs in C4-2-CM play essential roles in this process. Corroborative evidence for this also came from (1) MC3T3-E1 cells cultured with C4-2 EVs showed increased mineralization and active secretory autophagy (Figures 6c and S6h,i) and (2) increased number of MVBs, amphisomes in cell profile and ILVs incorporated in MVBs (Figure 6d,e). These data suggest that EVs from C4-2 can induce secretory autophagy in osteogenic lineage cells and promote their production of LC3+ EVs.

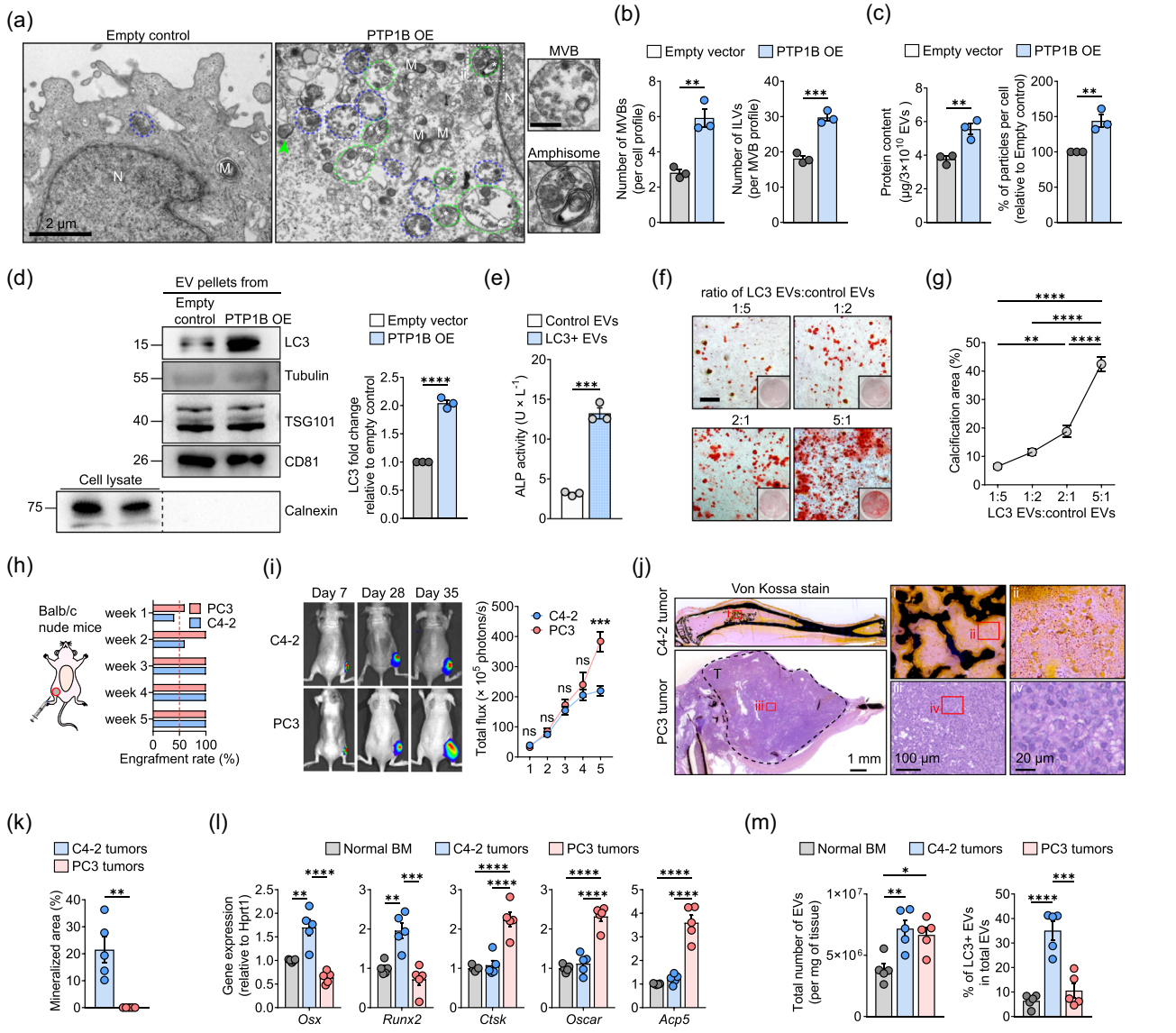

FIGURE 5 Osteoblastic LC3+ EVs from secretory autophagy pathway initiate early mineralization. **(a)** Representative TEM images of in empty control and PTP1B OE MC3T3-E1 cells. MVBs are indicated by blue dashed lines. Amphisomes are indicated by green dashed lines. Asterisks label autophagic cargos inside autolysosomes. Green arrows indicate autophagic cargos in the cytoplasm. Examples of individual MVB and amphisome are depicted (corresponding to i and ii at the right panel). N, nucleus. M, mitochondrion. Scale bars, 2 μm (left); 500 nm (right). **(b)** Quantification shows the number of MVBs per cell profile and the number of ILVs per MVB profile in (**a**). $n = 3$ biological replicates. Each dot indicates a mean value from 3 to 5 individual cells. **(c)** Left, quantitative protein content of EV fraction from PTP1B OE MC3T3-E1 cells. Right, quantification shows concentration of particles from PTP1B OE MC3T3-E1 cells relative to empty control MC3T3-E1 cells. $n = 3$ biological replicates. **(d)** EV samples were collected from PTP1B-overexpressing cells. Left, western blot analysis was performed examining LC3, Tubulin, TSG101, CD81 and Calnexin. Right, quantitative analysis of LC3 fold change relative to empty control cells. $n = 3$ biological replicates. **(e)** LC3+ EVs were isolated from PTP1B OE MC3T3-E1 cells and assayed for ALP activity. Control EVs represent EVs from empty vector-transfected MC3T3-E1 cells. $n = 3$ biological replicates. **(f)** Representative ARS staining images of MC3T3-E1 cells cultured with 3×10^8 mixed EVs for 10 days of osteogenic induction. The mixed EV populations were generated by combining LC3+ EVs with control EVs at ratios of 1:5, 1:2, 2:1, and 5:1, respectively. Scale bars, 200 μm. **(g)** Quantification shows the percentage (%) of calcification area in (f). $n = 3$ biological replicates. **(h)** Left, schematic of intratibial inoculation of tumour cells. Right, engraftment rate of C4-2 and PC3 cell lines in this mouse model. $n = 5$ mice per group. **(i)** Left, representative bioluminescence images of mice inoculated with C4-2 and PC3 for 7, 28 and 35 days. Right, quantification shows the luciferase intensities of grafted C4-2 and PC3 tumours by bioluminescence imaging. $n = 5$ mice per group. **(j)** Representative Von Kossa staining images of mouse tibias inoculated with C4-2 and PC3 for 28 days. Examples of osteogenic lesions in the bone marrow niche of C4-2 tumours are depicted, while PC3 tumours do not exhibit a phenotype of osteogenic lesions (corresponding to i and iii from left image). Examples of calcified nodules located in the extracellular matrix are depicted (corresponding to ii and iv from left image). Scale bars, 1 mm (left), 100 μm (middle), and 20 μm (right). **(k)** Quantification shows the percentage (%) of mineralized area within the osteogenic lesions in (j). $n = 5$ mice per group. **(l)** RT–qPCR analysis shows mRNA levels of osteogenic markers (*Osx*, *Runx2*) and osteoclast-relative (*Ctsk*, *Oscar*, *Acp5*) genes in C4 and PC3 tumours 28 days post inoculation. Each dot represents three technical replicates of the assay. $n = 5$ mice per group. **(m)** Left, quantification shows the EV distribution in C4-2 and PC3 tumours. Mice were euthanized 28 days post inoculation, then tumours were harvested and analysed for EV accumulation per mg of tissue. Normal bone marrow from Balb/c nude mice was used as a control. Right, the percentage (%) of LC3+ EV proportion in total EVs extracted from C4-2 and PC3 tumours. $n = 5$ mice per group. **(b–e,g,i,k–m)** Data are presented as mean values ± s.e.m.; two-sided unpaired *t*-tests **(b–e,k)**; one-way ANOVA with Tukey's post hoc test for multiple comparisons **(g,l)**; two-way ANOVA with Tukey's post hoc test for multiple comparisons (**i**). $^{****}p < 0.0001$, $^{***}p < 0.0005$, $^{**}p < 0.005$ and $^{*}p < 0.05$.

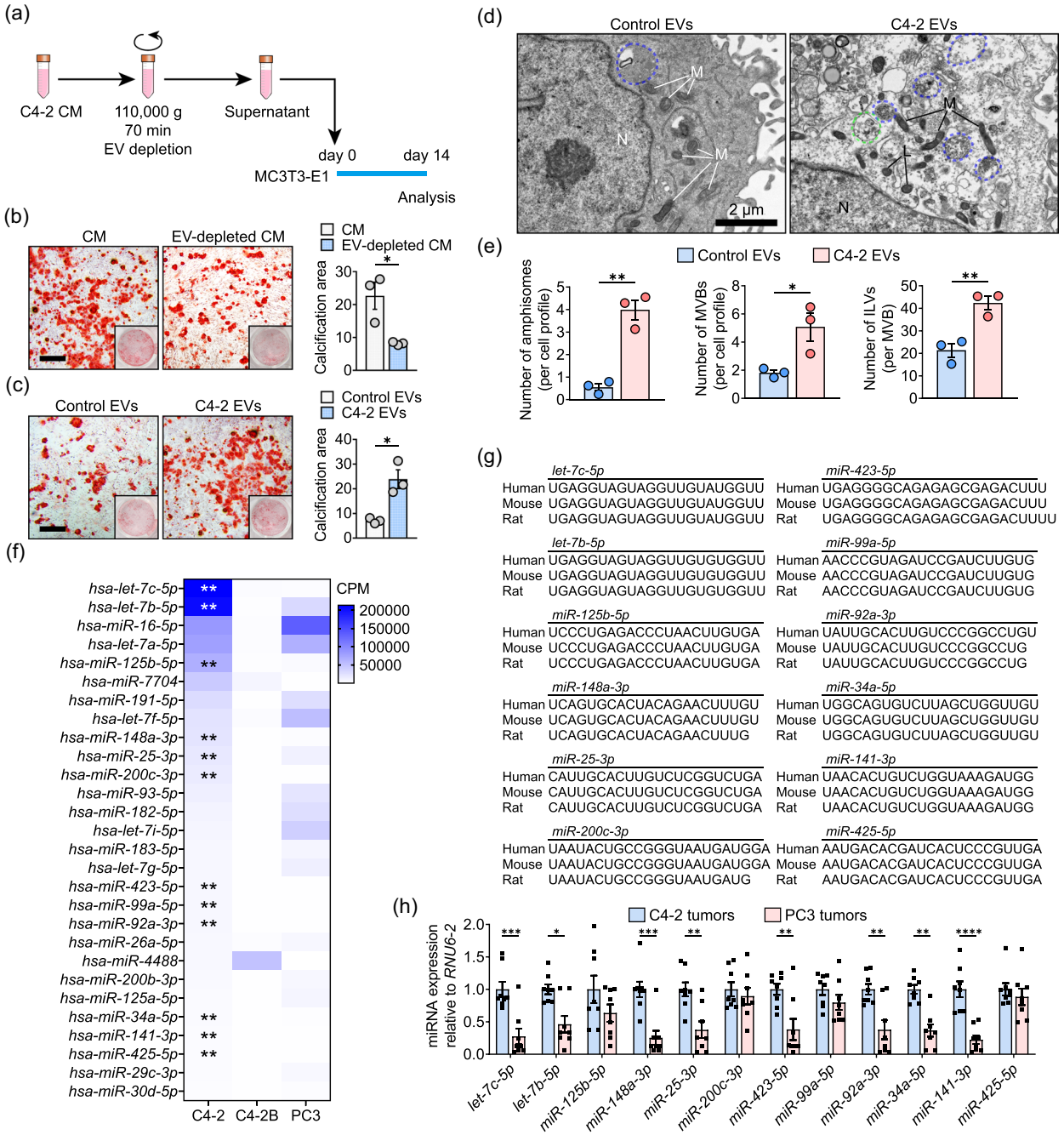

FIGURE 6 Tumoral EVs induce LC3+ EV generation from osteoblasts. **(a)** Schematic shows MC3T3-E1 cells were cultured with EV-depleted C4-2 CM during 14 days of osteogenic induction. **(b)** Left, representative ARS staining images of MC3T3-E1 cells cultured with C4-2 CM in the absence or presence of EVs. Scale bars, 200 μm. Right, the percentage (%) of calcification area was quantified. $n = 3$ biological replicates. **(c)** Left, representative ARS staining images of MC3T3-E1 cells cultured with 3×10^8 C4-2 EVs. Scale bars, 200 μm. Right, the percentage (%) of calcification area was quantified. $n = 3$ biological replicates. EVs from PC3 were used as control. **(d)** Representative TEM images of MC3T3-E1 cells cultured with 3×10^8 C4-2 EVs. MVBs are indicated by blue dashed lines. Amphisomes are indicated by green dashed lines. N, nucleus. M, mitochondrion. Scale bars, 2 μm. **(e)** Quantification shows the number of amphisomes and MVBs per cell profile, and the number of ILVs per MVB profile in (**d**). $n = 3$ biological replicates. Each dot indicates a mean value from 3 to 5 individual cells. **(f)** A heatmap shows top 28 microRNAs expressed in C4-2 EVs. Double asterisks label the microRNAs specifically enriched in C4-2 EVs. CPM, counts per million. **(g)** Sequence alignment analysis of 12 microRNAs specifically enriched in C4-2 EVs reveal their evolutionary conservation across mammals. **(h)** Expression levels of 12 microRNAs in C4-2 and PC3 tumours were detected 28 days post inoculation. Each dot represents three technical replicates of the assay. $n = 8$ mice per group. **(b,c,e,h)** Data are presented as mean values ± s.e.m.; two-sided unpaired *t*-tests **(b,c,e)**; multiple unpaired *t* tests (**h**). $^{****}p < 0.0001$, $^{***}p < 0.0005$, $^{**}p < 0.005$ and $^{*}p < 0.05$.

Given the high abundance of miRNAs in EVs, we speculated that miRNAs encapsuled in C4-2-EVs may play a role in this process. To explore further, we extracted total miRNAs of EVs and performed miRNA-seq using Illumina NovaSeq 6000 (Ma et al., 2021). A cluster of miRNAs was highly enriched in EVs from C4-2 and conserved across human, mouse and rat (Figure 6f,g). A panel of eight miRNA signatures including let-7b-5p, let-7c-5p, miR-148a-3p, miR-25-3p, miR-423-5p, miR-148a-3p, miR-92a-3p, miR-34a-5p, miR-141-3p was screened, based on their expression in both EV fractions and tumour grafts (Figures 6h and S6j). Pathway and network analysis confirmed a close association between mRNA targets of these signatures and biological processes including extracellular secretion, osteogenic mineralization, vesicular transport, and autophagy (Figure S6k,l). These results suggest that C4-2 EVs possess a specific panel of miRNA signatures that may play essential roles in activating the secretory autophagy pathway in osteogenic lineage cells.

2.8 | Ablation of tumoral *RAB27A* expression or osteoblastic *Ptpn1* knockdown reduces tumour-associated bone remodelling

Finally, we investigated whether the tumoral EV secretion or osteoblastic PTP1B expression and the tumour-associated bone remodelling were causally linked. If that were the case, we reasoned that genetic ablation of tumour EVs or osteoblastic PTP1B might rescue the aberrant bone remodelling and lesions caused by the excessive release of LC3+ EVs. To test this hypothesis, we targeted *RAB27A* expression, a key regulator of EV secretion (Ostrowski et al., 2010), in C4-2 cells via short hairpin RNA (Figure S7a). Consistent with previous results (Wang et al., 2023), *RAB27A* loss suppressed EV secretion by tumour cells without altering size distribution and morphology of EVs (Figure S7b-d). *RAB27A* ablation in C4-2 reduced both the total number of EVs in tumour tissues and the LC3+ EV proportion in total EVs, despite unaltered tumour growth both in vitro and in vivo (Figures 7a,b and S7e,f). Osteoblastic lesions and mineralized nodules were markedly reduced in mice bearing *RAB27A*-knockdown tumours compared with controls with similar tumour burdens (Figures 7c,d and S7f), highlighting that tumour-derived EVs are crucial for aberrant bone remodelling and lesions. In another separate experiment, we specifically ablated osteoblastic *Ptpn1* using an adeno-associated serotype 2 virus (AAV2) viral vector via intratibia injection (Figures 7e and S7g). While AAV transfection had no effect on tumour growth (Figure S7h), osteoblastic *Ptpn1* ablation significantly decreased EV abundance in tumours and LC3+ EV proportion in total EVs and reduced osteoblastic destruction in tumour tissues, as compared with either AAV2-OSX vector or PBS controls (Figure 7f–h). Together, these findings indicate that tumour-associated bone remodelling is not merely controlled by the overall amount of LC3+ EV production in the bone metastatic niche. Instead, osteoblastic *Ptpn1* could specifically enhance the secretory autophagy pathway, a process that is initiated by tumoral EVs in the bone metastatic niche.

3 | DISCUSSION

In this study, we show that tumoral EVs induce secretory autophagy in osteoblasts, leading to osteoblastic mineralization and the development of osteogenic lesions in the bone marrow niche (Figure 7i). Mechanistically, tumoral EVs with a cluster of specific miRNAs can boost PTP1B expression in osteogenic lineage cells, and switch the autolysosome pathway to the secretory pathway by PTP1B-mediated STX17 dephosphorylation at Tyr157 and Tyr227 residues, thus driving LC3+ EV secretion and mineralization. Blocking EV secretion by ablating *RAB27A* in tumour cells, or blocking osteoblastic PTP1B expression rescues these phenotypes. Notably, we show that osteoblastic LC3+ EVs, the specific EVs generated through the secretory autophagy pathway, are the primary contributor to tumour-associated bone remodelling.

3.1 | Autophagosome-lysosome fusion governed by PTP1B-STX17 axis

Interaction between STX17, SNAP29, and VAMP8 was previously reported (Itakura et al., 2012), although how this SNARE complex formed remains unknown. We confirmed that increased phosphorylation of STX17 at Tyr157 and Tyr227 residues promotes autolysosome formation in sg*PTPN1* cells. The STX17-Y2F mutation in sg*PTPN1* cells blocked the formation of STX17-SNAP29-VAMP8 SNARE complex (Figure 3), raising a possibility that increased phosphorylation of Tyr157 and Tyr227 residues may alter the STX17 conformation and enhance its binding to SNAP29. However, the STX17-Y2E mutation neither increased the binding capacity of STX17 to SNAP29 and VAMP8, nor increased lysosomal volume, suggesting that most of Tyr157 and Tyr227 residues have been phosphorylated by *PTPN1* knockout. Our data both confirm the robustness of STX17 dephosphorylation regulated by PTP1B, and show that phosphorylation of STX17 at Tyr157 and Tyr227 residues is indispensable for the SNARE complex formation. Given the known subcellular localization, it is likely that PTP1B on the ER surface (Eden et al., 2010) can directly contact and dephosphorylate STX17 on the surface of completed autophagosomes (Itakura et al., 2012). It is conceivable that autophagosome-lysosome fusion will still be blocked by PTP1B overexpression, even if the binding of SNAP29 to VAMP8 on the lysosomal surface is not affected (Figure 7j).

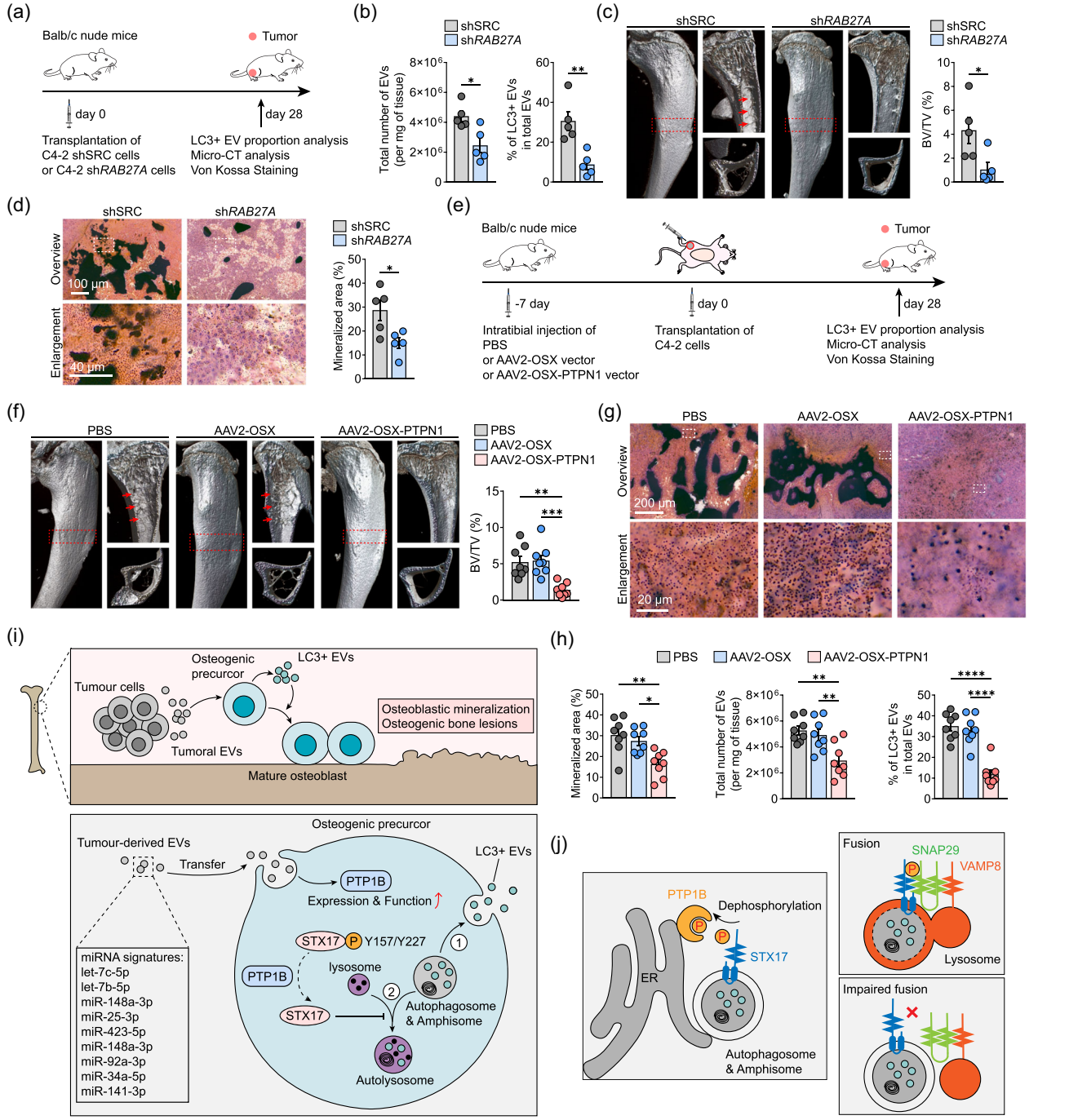

FIGURE 7 Ablation of tumoral *RAB27A* expression or osteoblastic *PTPN1* knockdown reduce tumour-associated bone remodelling. **(a)** Schematic for the generation of mice bearing xenografts of sh*RAB27A* C4-2 human prostate cancer cells. Mice were euthanized 28 days after inoculation to assess the proportion of LC3+ EVs and osteogenic lesions. **(b)** Left, quantification shows the EV distribution in shSRC and sh*RAB27A* C4-2 tumours. Mice were euthanized, and tumours were harvested to analyse EV accumulation per mg of tissue. Right, the percentage (%) of LC3+ EV proportion in total EVs extracted from shSRC and sh*RAB27A* C4-2 tumours. $n = 5$ mice per group. **(c)** Left, representative micro-CT images of tibias inoculated with shSRC and sh*RAB27A* C4-2 cells for 28 days. Red arrows point to ectopic osteoblastic lesions within the bone marrow cavity. Right, quantification of trabecular bone volume fraction (BV/TV) of regions of interest (indicated by red dashed boxes in left panel). **(d)** Left, representative Von Kossa staining images of mouse tibias inoculated with shSRC and sh*RAB27A* C4-2 cells for 28 days. Examples of osteogenic lesions in the bone marrow niche of C4-2 tumours are depicted in overview. Examples of calcified nodules located in the extracellular matrix are depicted are depicted in enlargement. Scale bars, 100 μm (overview), 40 μm (enlargement). Right, the percentage (%) of mineralized area within the osteogenic lesions was quantified. $n = 5$ mice per group. **(e)** The experimental procedure for osteoblast-specific *PTPN1* knockdown by AAV2 virus. Balb/c nude mice were given intratibial injection of AAV2-OSX-*PTPN1*, AAV2-OSX, and PBS 7 days before C4-2 inoculation to maximize the viral expression and knockdown efficiency. Mice were euthanized 28 days after inoculation to assess the proportion of LC3+ EVs and osteogenic lesions. **(f)** Left, representative micro-CT images of mouse tibias treated with AAV2-OSX-*PTPN1*, AAV2-OSX, and PBS. Red arrows point to ectopic osteoblastic lesions within the bone marrow cavity. Right, quantification of trabecular bone volume fraction (BV/TV) of regions of interest (indicated by red dashed boxes in left panel). **(g)** Representative Von Kossa staining images of mouse tibias treated with AAV2-OSX-*PTPN1*, AAV2-OSX, and PBS. Examples of osteogenic lesions in the bone marrow niche of C4-2 tumours are depicted in overview. Examples of calcified nodules located in the extracellular matrix are depicted are depicted in enlargement. Scale bars, 200 μm (overview), 20 μm (enlargement). **(h)** Left, quantification shows the percentage (%) of

(Continues)

FIGURE 7 (Continued)
mineralized area within the osteogenic lesions in **(e)**. Middle, quantification shows the EV distribution in tumours of the indicated group mice. Right, the percentage (%) of LC3+ EV proportion in total EVs extracted from tumours of the indicated group mice. $n = 8$ mice per group. **(i)** A model summarizing the central tenets of tumour-associated bone remodelling is demonstrated in the present osteogenic tumour cell models. In the bone metastatic niche, tumoral EVs can stimulate osteoblasts to enter a secretory autophagy state and generate LC3+ EVs. Osteoblastic LC3+ EVs generated through the secretory autophagy pathway serve as crucial contributor in tumour-associated bone remodelling by promoting mineralization. Mechanistically, PTP1B impedes the autophagosome-lysosome fusion by dephosphorylating STX17, while this molecular event redirects the cells from a canonical autophagic degradation to a secretory autophagy pathway. **(j)** A model of elucidating STX17 dephosphorylation and STX17-SNAP29-VAMP8 SNARE complex formation governed by PTP1B. Dephosphorylation of STX17 at Tyr157 and Tyr227 residues directly blocks SNARE complex formation and autophagosome-lysosome fusion. **(b–d,f,h)** Data are presented as mean values ± s.e.m.; two-sided unpaired *t*-tests **(b–d)**; one-way ANOVA with Tukey's post hoc test for multiple comparisons (**f,h**). $^{****}p < 0.0001$, $^{***}p < 0.0005$, $^{**}p < 0.005$ and $^{*}p < 0.05$.

In addition, we found that PTP1B knockout induces autophagosome maturation into autolysosome without concomitant alteration of lysosomal activity (Figure 1). Our results, together with previous evidence that either lysosomal acidification, or autophagosome-lysosome fusion can independently promote autolysosome formation (Mauvezin et al., 2015), suggesting that autophagosome-lysosome fusion mediated by PTP1B ablation is independent of lysosomal acidification.

3.2 | Factors and mechanisms affecting secretory autophagy

So far, limited knowledge is available on the causes and molecular mechanisms that regulate the rerouting of autophagosomes onto a pathway for extracellular release. Several studies proposed that bacterial and viral infections can activate secretory autophagy. Host cells release abundant virus-containing EVs via secretory autophagy pathway (van der Grein et al., 2022), while these EVs can transfer the infection to new host cells and evade immune surveillance as the EV membrane shields virions from recognition by neutralizing antibodies (Feng et al., 2013; Nagashima et al., 2017; van der Grein et al., 2022). As a result, secretory autophagy pathway can be activated by viruses to enhance infection efficiency. Conversely, infected cells release EVs acting as decoys that trap membrane-acting virulence factors to prevent damage of target tissues (Keller et al., 2020), or triggering antiviral immune responses in targeted cells to limit the infection spreading (Feng et al., 2015). To date, the molecular mechanisms involved in secretory autophagy are mainly attributed to autophagy machineries such as ATG proteins (Cadwell & Debnath, 2018; Keller et al., 2020), even though ATGs also control pathways that involve the formation of a classic autophagosome and terminate in lysosomal degradation (Cadwell & Debnath, 2018). In addition, a R-SNARE Sec22b in combination with STX3/4 and SNAP23/29 completes cargo selection during secretory autophagy (Kimura et al., 2017). Apart from these limited targets, the broader regulatory mechanisms of secretory autophagy remain unclear. We observed that PTP1B overexpression activates a secretory pathway by enabling autophagosomes to bypass STX17-dependent fusion with lysosomes, in which circumstance cells secrete more proteins and LC3+ EVs into the extracellular space. Our results highlight an intracellular adaptive mechanism whereby the secretory autophagy pathway is activated in response to autolysosomal inhibition.

We believe that LC3+ EVs are characteristic products of secretory autophagy. In wild type cells without any stimulation, a portion of LC3 can be naturally secreted as free protein into extracellular space, while these LC3 proteins are hardly encapsulated inside EVs (Figure 4b). In contrast, secretory autophagy activated by either upregulation of PTP1B (Figure 4b), or virus infection (van der Grein et al., 2022), leads to the secretion of LC3 as both free proteins and EV cargos. These observations, together with previous reports (Keller et al., 2020; Leidal et al., 2020; Yan et al., 2022), demonstrate that unconventional secretion is not only a way to discard waste in response to autolysosomal inhibition (Solvik et al., 2022) but also a highly selective process by which specific molecules are released and mediate corresponding signalling. Furthermore, we demonstrated the robustness of STX17 dephosphorylation by PTP1B in both HEK293T cells and MC3T3-E1. Our data substantiates the extensive stability of the PTP1B-STX17 axis across distinct cellular lineages and species, recapitulating the significance of PTP1B and STX17 in regulating secretory autophagy due to their highly conserved structure and function.

3.3 | Are LC3+ EVs analogous to MVs?

We confirmed that LC3+ EVs can initiate mineralization both in vivo and in vitro, which has a similar function to matrix vesicles (MVs). Since their discovery in 1967 (Anderson, 1967), MVs have been shown to be critical drivers in osteoid mineralization, while aberrant changes in MV function have also been confirmed in mineralization-associated bone diseases such as osteopetrosis (Wang et al., 2022). Although the nomenclatures are different, osteoblastic LC3+ EVs and MVs share similar characteristics (1) both can initiate mineralization and are correlated with aberrant mineralization; (2) the initial biogenesis of both comes from inward budding of endosomal membrane (i.e., exosomal pathway) (Rohde & Mayer, 2007; Yan et al., 2022); (3) both share a similar bilayer spherical morphology and a diameter of ~100 nm. However, osteoblastic LC3+ EVs still differ from MVs in certain

aspects. Traditional views regard MVs are secreted from cells with mineralization potential such as osteoblasts and chondrocytes through polarized budding and pinching-off of vesicles from specific regions of the outer plasma membranes (Anderson, 2003). In contrast, LC3+ EVs are released from the secretory autophagy pathway upon PTP1B regulation, and few LC3+ EVs originate from MVB pathway (Figures 4 and 5). Therefore, we propose that osteoblastic LC3+ EVs are likely to be an unconventional type of MVs derived from the secretory autophagy pathway that still possess mineralization potential. Whether secretory autophagy-mediated LC3+ EV secretion is involved in bone development and physiological mineralization remains to be systematically elucidated.

3.4 | Strategies for restoring the homeostasis of the bone marrow niche

We and others have found that the 'vicious cycle' of metastatic osteolysis is attributed not only to the fact that tumour cells induce the differentiation and release of RANKL by osteoblasts, but also to the direct activation of osteoclastogenesis mediated by tumour-derived cytokines and EVs (Croucher et al., 2016; Ma et al., 2021; Sturge et al., 2011). Intriguingly, we also found that C4-2 increased trabecular bone density in the tibial marrow cavity of tumour-bearing mice (Ma et al., 2021). Hence, we do not exclude the possibility that due to tumour heterogeneity, distinctions between cytokines or EV profiles of tumours can lead to opposite bone destruction phenotypes and clinical outcomes, especially considering the effects of autophagy, inflammation, and tumour growth. Indeed, we provide evidence that tumoral EVs can switch osteoblastic state from lysosomal degradation to unconventional secretion, thus building osteogenic bone lesions in the bone marrow niche (Figure 6). Strategies that stabilize osteoblast function are essential to minimize side effects of bone depositions induced by bone tumours and metastases. As we have demonstrated that tumoral EVs-induced PTP1B upregulation boosts secretory autophagy pathway and disrupts bone homeostasis, and that targeting osteoblastic PTP1B may restore homeostasis in the bone marrow niche (Figure 7). Strategies to reduce tumoral EV secretion should also be considered, as they may inhibit tumours from hijacking bone-resident cells to create a tumour microenvironment that impedes therapy.

4 | METHODS

4.1 | Cell culture

Human embryonic kidney 293 cell line HEK293T, mouse osteoblast precursor cell line MC3T3-E1, human prostate cancer cell lines C4-2, C4-2B, and PC3 were purchased from ATCC. Cells were cultured in 90% DMEM high glucose medium (Hyclone) with 10% foetal bovine serum (Gibco) and 1% penicillin-streptomycin (Hyclone), and maintained in a 37°C incubator containing 5% CO2-enriched atmosphere. The absence of mycoplasma contamination was confirmed in all cell lines.

4.2 | Lentivirus and adenovirus transfection

CAS9-easy-lentivirus used to knockout PTPN1 (sgSCR-1, sgSCR-2, sgPTPN1-1, sgPTPN1-2, and sgPTPN1-3) were constructed by Shanghai Genechem Co., Ltd. *RAB27A* knockdown in C4-2 cells was achieved by infecting cells using lentivirus (pLKO.1, sh*RAB27A*, TRCN0000005295, Sigma). The information of oligonucleotide sets and plasmids was listed in Table S1. To generate stable cell lines, 5×10^4 cells were seeded in 6-well plates and transfected with lentivirus mixed with polybrene (MedChemExpress). After 48 h of transfection, the stable expression cell lines were selected with puromycin (Sigma–Aldrich; 5 μg/mL) for at least 2 weeks. For mCherry-EGFP-LC3 autophagy reporter system, an adenovirus expressing mCherry-EGFP-LC3 fusion protein (Beyotime Biotechnology) was used to infect cells following the manufacturer's instructions. Briefly, cells were seeded in confocal dishes at a density of 1×10^5 cells per well and cultured overnight at 37°C in 5% CO_2 incubator. When the cells reached 50% confluence, the mCherry-GFP-LC3B adenovirus (1×10^8 pfu/mL) was added according to the MOI of the cells. After, 24 h of infection, 2 mL complete culture medium was added to each well. Cell autophagy was observed with a confocal microscope (Zeiss, LSM-880).

4.3 | Treatment of MC3T3-E1 cells

To assess the osteogenic potential of LC3+ EVs, MC3T3-E1 cells were cultured for 10 days in osteogenic medium containing 3×10^8 mixed EV populations generated through combining LC3+ EVs with control EVs at ratios of 1:5, 1:2, 2:1, and 5:1, respectively. To assess the osteogenic potential of EVs, MC3T3-E1 cells were cultured with EV-depleted CM or EVs of osteogenic induction. CM from cultured tumour cells, or EV-depleted CM obtained after EV isolation (i.e., the media supernatant after first

spin of 110,000 g for 70 min as described above), was concentrated using Amicon Ultra-15 centrifugal filters with 10 kDa cutoff (Millipore, UFC901024) at 4000 g at 4°C. Generally, 1 mL of CM from cell culture contains approximately 3×10^9 of EVs. The same concentration of CM, or EV-depleted CM was further used to culture MC3T3-E1 cells for 7 or 14 days. For EV treatment, MC3T3-E1 cells were cultured with 3×10^9/mL EVs, consistent with the EV concentration in CM, for 14 days of osteogenic induction. At the indicated time point, the cells were collected for RNA extraction, RT-qPCR analysis, TEM analysis, and Alizarin Red S staining; the cell supernatant was collected for EV isolation and LC3+ EV proportion analysis. For Alizarin Red S staining, cells induced for 10 or 14 days were washed with PBS, and fixed in 4% PFA for 20 min, and stained using the Alizarin Red S staining Kit (Beyotime Biotechnology) following the manufacturer's instructions. ALP activity was assessed using the Alkaline Phosphatase Assay Kit (Abcam, ab83369) according to the manufacturer's instructions. In detail, MC3T3-E1 cells were cultured with 3×10^8 LC3+ EVs or control EVs for 7 days of osteogenic induction, respectively. The cells were subsequently washed with PBS three times, followed by the addition of the pNPP solution. After incubation at 25°C for 60 min, stop solution was added. ALP activity was examined with microplate reader at 405 nm.

4.4 | Immunofluorescence

For immunofluorescence staining, cells were seeded into confocal dishes and divided into groups for treatment. Fix cells at room temperature with 4% paraformaldehyde for 20 min, followed by permeabilization using 0.1% Triton X. After blocking with 5% BSA for 30 min, cells were incubated with the primary antibody overnight at 4°C. After washing with PBS for three times, the cells were incubated with fluorescent-conjugated secondary antibodies for 1 h in the dark. All samples were treated with DAPI dye for nuclear. After additional washes in PBS, images were captured using a confocal scanning microscope (Zeiss, Jena, Germany).

4.5 | Co-immunoprecipitation (Co-IP) assay

To investigate the effect of blocking PTPs on tyrosine phosphorylation of STX17, cells were treated with 10 or 100 μM pervanadate for 15 min and immunoprecipitated with anti-STX17 antibody. To investigate the effect of *PTPN1* on tyrosine phosphorylation of STX17, sg*PTPN1* or sgSCR cells were lysed and immunoprecipitated by anti-PTP1B, anti-STX17 antibodies, or normal IgG as a negative control. To specifically investigate the phosphorylated residues of STX17, sgSCR and sgPTPN1 cells transfected with WT, Y157F, Y227F, or Y2F mutants of STX17 were immunoprecipitated with anti-FLAG antibody and subjected to western blot analysis.

Co-IP assay was performed using an rProtein A/G magnetic IP/Co-IP Kit (ACE Biotechnology). After the aforementioned treatment, cells were lysed using 1 × enhanced lysis/wash buffer and incubated for 15 min on ice. The cell lysate samples were collected by centrifugation at 13,000×*g* for 10 min. Total lysates (200 μg; 1 μg/μL) were incubated with 4 μL of indicated primary antibodies or normal IgG for 30 min. Subsequently, the samples were mixed and incubated with prepared rProtein A/G magnetic beads for 2 h at room temperature. Beads were then rinsed three times in 1 × washing buffer, resuspended in 50 μL of loading buffer, and heated in metal bath at 100°C for 5 min. The immunoprecipitate was loaded on SDS-PAGE and western blot analysis was performed using relative antibodies.

4.6 | Lysosomal activity and pH measurement

The Lysosomal pH was determined using BBcellProbe lysosome pH detection kit in accordance with the manufacturer's instructions. Briefly, sgSRC and sgPTPN1 cells were plated in a 96-well plate. Following cell static adherence, replace the BBcellProbeTM P02 staining solution and incubate at 37°C for 1–5 min. Subsequently, measure the fluorescence intensity using a microplate reader. The pH values were calculated according to the standard pH curve. For Lysosensor test, cells were incubated with 5 μM LysoSensor Green DND-189 (Shanghai Maokang Biotechnology Co., Ltd., MX4321-50UL) for 90 min at 37°C and washed using PBS for two times. Hoechst 33342 was used to stain the nuclei for 10 min, followed by washing twice.

4.7 | Acid phosphatase assay

The isolation of lysosomes was conducted in accordance with the manufacturer's instructions (Sigma–Aldrich, LYSISO1). Briefly, a total of 3×10^8 cells were trypsinized and centrifuge at 600 g for 5 min to discard the supernatant. The cells were resuspended in a 2.7 packed cell volume of 1 × extraction buffer and subsequently disrupted using a Dounce homogenizer with pestle. Crude lysosomal fractions were isolated by centrifugation and collect the pellet in a minimal volume of 1 × extraction buffer (~0.4 mL per 10^8 cells). The purification of lysosomes from the crude lysosomal fraction was achieved through density gradient

centrifugation at 150,000 × g for 4 h on an OptiPrep density gradient. Acid phosphatase activity was then measured with Acid Phosphatase Assay Kit (Sigma-Aldrich, CS0740) by following the manufacturer's instructions. In brief, pre-warmed substrate solution and reaction components were mixed in a 96-well plate. The ACP2 activity was determined by adding 50 μL of assay buffer to 50 μL of test sample. The plates were incubated at 37°C for a duration of 5–10 min, followed by the addition of 200 μL of stop solution to each well to terminate the reaction. Subsequently, absorbance value at 405 nm was measured, and acid phosphatase activity was calculated.

4.8 | Western blot

EV pellets isolated from shPTPN1 and shSRC cells were resuspended in PBS and treated with 50 μg/mL proteinase K (Thermo Scientific, EO0491) in the absence or presence of 0.2% triton for 30 min on ice. The reaction was terminated by the addition of 1 mM PMSF. Then, samples were collected and suspended in RIPA buffer (Thermo-Scientific) containing 10 × protease inhibitor and phosphatase inhibitor. The protein contents of both cell lysate and EV fraction were determined using the BCA assay kit (23225, Thermo Fisher Scientific). Protein samples or immunoprecipitate samples were loaded on SDS-PAGE for separation, transferred onto a PVDF membrane, and blocked with 5% BSA for an hour. The membranes were subsequently incubated with primary antibodies at a dilution of 1:1000 overnight at 4°C. The detailed antibody information is as follows: mouse monoclonal anti-PTP1B (abcam, ab244207), rabbit monoclonal anti-STX17 (abcam, ab316119), mouse monoclonal anti-phospho-tyrosine (Cell Signalling Technology, #9411), rabbit monoclonal anti-VAMP8 (abcam, ab76021), rabbit monoclonal anti-SNAP29 (abcam, ab181151), rabbit monoclonal anti-Flag (abcam, ab205606), rabbit monoclonal anti-LC3B (ABclonal, A15591), mouse monoclonal anti-GAPDH (abcam, ab8245), rabbit polyclonal anti-Tubulin (ABclonal, AC015), rabbit monoclonal anti-TSG101 (abcam, ab125011), rabbit polyclonal anti-CD81 (ABclonal, A5270), rabbit monoclonal anti-Calnexin (ABclonal, A15631). The membranes were then washed with TBST for three times and probed with secondary antibodies goat anti-rabbit IgG H&L (abcam, ab205718) or goat anti-mouse IgG H&L (abcam, ab205719) at room temperature for an hour. After washing with TBST, the membranes were treated with Clarity ECL Substrate (Bio-Rad, #1705060) and subsequently detected using a ChemiDoc imager (Bio-Rad).

4.9 | RT–qPCR

Tumours were segmented into small pieces and immersed in 2 mL TRIzol reagent, and cell lines were lysed in RLT buffer and stored at −80°C. Tissue homogenization was performed using a low-temperature tissue grinder machine. The supernatant was collected by centrifugation at 12,000 g for 10 min at 4°C. Total RNA was isolated by a RNeasy Plus Mini Kit (QIAGEN, 74134), and RNA concentration was measured using NanoDrop2000. The cDNA was synthesized by reverse transcription using PrimeScript RT Reagent Kit. SYBR Premix Ex Tag II was used for PCR reaction. The primer sequences were listed in Table S2.

4.10 | Isolation of EVs

Cells were cultured in EV-depleted medium generated by supplementing DMEM with 10% EV-depleted FBS for 24 h before EV isolation. EV-free FBS was either produced in-house by ultracentrifugation of serum at 110,000 g for 16 h and passed through a 0.22 μm filter or purchased from Systembio (Cat.no EXO-FBS-50A-1). The supernatant was collected and centrifuged at 1000 g for 15 min, 3000 g for 20 min, 12,000 g for 30 min to remove cell debris, apoptotic bodies and large microvesicles, respectively. The supernatant was further ultracentrifuged at 110,000 g for 70 min (Beckman Coulter) with a SW40 rotor (k-factor: 280.3). The pelleted EVs were resuspended with DMEM and loaded over 30% sucrose solution (diluted with D_2O) slowly without mixing the two layers, and centrifuged at 110,000 g, 4°C for 2 h. The supernatant was subsequently discarded, and the sucrose layer was resuspended in PBS followed by ultracentrifuged at 110,000 g for 70 min to pellet down the EVs. To isolate EVs from bone marrow, bone marrow fluid collected by washing the medullary cavities of the tibias was filtrated through a 0.2 μm filter and subjected to differential ultracentrifugation in combination with sucrose cushion ultracentrifugation. For extract EVs from the tissue, femurs and tibias were dissected and the attached muscles and periosteum were cleaned under sterile condition. The tissue samples were subsequently weighed and documented. Then the epiphyses were removed and bone marrow was thoroughly flushed out with α-MEM. The remaining samples of bone tumours were physically crashed to small pieces using a tissue homogenizer and then subjected to digestion by collagenase and DNase I (30 μg/mL; Roche) for 30 min at 37°C. The bone marrow and tissue suspension was filtered through a 70 μm cell strainer, followed by centrifugation at 1000 g for 15 min, 3000 g for 20 min, and finally at 12,000 g for 30 min to effectively remove cellular components, tissue debris, apoptotic bodies, and large microvesicles. Subsequently, EVs were isolated with ultracentrifugation and sucrose ultracentrifugation techniques. EV size and number were analysed with the NanoSight NS300 characterization system (NanoSight, UK). EVs were imaged by negative-stain transmission electron microscopy. For the quantification of LC3+ EVs, 1×10^8 NTA-based EVs resuspended in 100 μL PBS were incubated with

5 μL anti-LC3 antibody for 1 h at 4°C. The particles were then pelleted, collected, and incubated with 5 μL secondary antibody for 30 min at 4°C. LC3 detection was performed using a flow cytometer (CytoFLEX, Beckman Coulter, Brea, CA, USA). The proportion of LC3+ EVs was quantified using the FlowJo 10.0 software.

4.11 | Transmission electron microscope

Cells (1–5 × 10^5 per mL) were centrifugated at 1200 rpm for 5 min and then incubated with the fixation buffer including 2.5% glutaraldehyde (Solarbio) for 2 h and 1% OsO4 for 30 min. After being washed with PBS three times, the cells were subsequently dehydrated using a sequential gradient of acetone (50%, 70%, 90%, and finally 100%), followed by embedded in epoxy resin prior to sectioning into thin slices measuring 50–70 nm. The slices were stained with 2% uranyl acetate and lead citrate for 15 min at room temperature, dried naturally, and viewed with a Tecnai 20 (FEI).

4.12 | Bioinformatics analysis

For protein interaction analysis, protein sequences were obtained from UniProt to generate heterodimer models between full-length PTP1B and target SNAREs or autophagic receptors (entry IDs: PTP1B: P18031; STX17: P56962; STX7: O15400; STX8: Q9UNK0; SNAP29: O95721; VIT1B: Q9UEU0; VAMP3: Q15836; VAMP7: P51809; VAMP8: Q9BV40; YKT6: O15498; TBK1: Q9UHD2; FAM134B: Q9H6L5; FAM134C: Q86VR2), using AlphaFold-Multimer algorithm (protein sequences available in Table S3). A predicted DockQ ≥ 0.23 represents an acceptable binding possibility between proteins. The molecular 3D binding model of PTP1B and STX17 was visualized using PyMOL. Predicted polar contacts within 3 Åm were analysed and visualized a customized script in PyMOL.

4.13 | Animal experiments

All animal breeding and experimental procedures were performed in accordance with protocols approved by the Institutional Animal Care and Use Committee of Third Military Medical University. Male Babl/c nude mice (6–8 weeks old) were obtained from Laboratory Animal Centre of Third Military Medical University (Chongqing, CHINA). Mice were housed in a light-, humidity-, temperature-controlled, and pathogen-free environment (lights were on from 06:00 to 18:00, 40%–70% humidity, and 21–25 °C temperature).

For intratibial inoculation, 6–8 weeks old BALB/c nude mice were immobilized with the knee flexed, and 2 × 10^5 luciferase-labelled C4-2 and PC3 cells resuspended in 50 μL of PBS were injected into the marrow cavity through the tibial plateau using an insulin syringe. BLI was performed every week to monitor tumour growth. After 28 days of inoculation, mouse tibias were collected for histological analysis. The tumour tissues were simultaneously collected for RT–qPCR analysis and EV isolation. To investigate the effect of EV secretion from tumours on bone remodelling, 6–8 weeks old BALB/c nude mice were intratibially inoculated with 2 × 10^5 shSRC or sh*RAB27A* C4-2 cells resuspended in 50 μL of PBS. After 28 days of inoculation, mice were euthanized and tissue samples were collected for the assessment of LC3+ EVs and osteogenic lesions. To specific knock-down the mouse osteoblastic *Ptpn1*, a recombinant AAV2 viral vector (AAV2-*Osx*-*Ptpn1*) encoding *Ptpn1* shRNA in concert with osteoblast-specific promoter (*Osx*) was created. Male BALB/c nude mice aged 6–8 weeks were intratibially injected with 20 μL of AAV2-*Osx*-*Ptpn1* or AAV2-*Osx* viral solution (1 × 10^{11} vg/mL) 7 days prior to tumour inoculation (defined as day–7). The negative control mice received an equivalent volume of PBS. After 7 days, 2 × 10^5 C4-2 cells were intratibially injected into BALB/c nude mice, and grown for 28 days. Mice were euthanized and samples were collected for analysis of LC3+ EV proportion and bone remodelling. For BLI imaging, mice were intraperitoneally injected with D-fluorescein (150 mg/kg) 10 min prior to imaging. The introductory anaesthesia involved the use of a 3% isoflurane-oxygen mixture, while a 1.5% mixture was employed for maintenance anesthesia. Imaging was performed with an AniView100 (Biolight Biotechnology). Luciferase intensities of the region of interest over the tumour were quantified as total flux (photons/s) with AniView software. For section staining, mouse tibias were harvested following the removal of skin and muscle, fixed with 4% paraformaldehyde for 48 h, and subsequently decalcified with EDTA for 4 weeks at room temperature. Tissues were dehydrated sing a sequential gradient of ethanol (30%, 50%, 70%, 95%, and finally 100%), subsequently embedded in paraffin, and sectioned into slices of 5 μm. The sections were dried at 60°C for an hour, deparaffinized using Histo-Clear dewaxing reagent, rehydrated, and incubated with 0.3% hydrogen peroxide to block endogenous peroxidase activity, followed by blocking with 10% FBS. For PTP1B immunohistochemistry, sections were incubated with rabbit anti-PTP1B (1:200, Abcam) overnight at 4°C, and then incubated with ImmPRESS horseradish peroxidase (HRP) anti-mouse IgG for 40 min at 37°C. Subsequently, sections were incubated with ImmPACT DAB Peroxidase (Vector Labs) for 10 min and the reaction was stopped by distilled water. For Von Kossa staining, tibias were fixed in 4% paraformaldehyde for 48 h, followed by resin embedding and sectioning into 10 μm slices. Subsequently, the sections were incubated with 5% silver

nitrate solution for 40 min, washed thrice with distilled water, and finally incubated with a 5% sodium hyposulfite solution for 2 min. The mineralized area was quantified using ImageJ software.

4.14 | Statistical analysis

Statistical analyses and graphing in this study were performed using GraphPad Prism software (Version Prism 9.4.0). Values are expressed as mean± s.e.m. Number of animals or independent replicates are denoted in the figure legend. A Student's two-sided *t*-test was performed for two-group comparisons. Multiple comparisons were performed using an ANOVA test followed by Dunnett's or Tukey's post hoc tests for intergroup comparisons. $p < 0.05$ were considered statistically significant.

AUTHOR CONTRIBUTIONS

Conceptualization, Qinyu Ma; methodology, Xiaoyu Wei, Mengmeng Liang, and Qinyu Ma; software, Qinyu Ma; formal analysis, Xiaoyu Wei, Mengmeng Liang, Min Deng, Ji Zheng, Fei Luo, and Qinyu Ma; investigation, Xiaoyu Wei, Mengmeng Liang, Qinyu Ma; resources, Fei Luo, and Qinyu Ma; writing—original draft, Xiaoyu Wei, Mengmeng Liang, and Qinyu Ma; writing—review & editing, Xiaoyu Wei, Mengmeng Liang, and Qinyu Ma; visualization, Qinyu Ma; supervision, Fei Luo, and Qinyu Ma; project administration, Fei Luo and Qinyu Ma; funding acquisition, Mengmeng Liang, and Qinyu Ma.

ACKNOWLEDGEMENTS

This work was supported by a grant from the National Natural Science Foundation of China (82202710 to Qinyu Ma), a grant from the National Natural Science Foundation of China (82302747 to Mengmeng Liang), and a grant from the Chongqing Postdoctoral Program for Innovative Talents (CQBX202202 to Qinyu Ma).

CONFLICT OF INTEREST STATEMENT

The authors report no conflict of interest.

ORCID

Qinyu Ma https://orcid.org/0000-0002-3817-6023

REFERENCES

Anderson, H. C. (1967). Electron microscopic studies of induced cartilage development and calcification. *The Journal of Cell Biology*, *35*(1), 81–101. https://doi.org/10.1083/jcb.35.1.81

Anderson, H. C. (2003). Matrix vesicles and calcification. *Current Rheumatology Reports*, *5*(3), 222–226. https://doi.org/10.1007/s11926-003-0071-z

Barahona, I., Rada, P., Calero-Pérez, S., Grillo-Risco, R., Pereira, L., Soler-Vázquez, M. C., LaIglesia, L. M., Moreno-Aliaga, M. J., Herrero, L., Serra, D., García-Monzon, C., González-Rodriguez, Á., Balsinde, J., García-García, F., Valdecantos, M. P., & Valverde, Á. M. (2022). Ptpn1 deletion protects oval cells against lipoapoptosis by favoring lipid droplet formation and dynamics. *Cell Death and Differentiation*, *29*(12), 2362–2380. https://doi.org/10.1038/s41418-022-01023-x

Bel, S., Pendse, M., Wang, Y., Li, Y., Ruhn, K. A., Hassell, B., Leal, T., Winter, S. E., Xavier, R. J., & Hooper, L. V. (2017). Paneth cells secrete lysozyme via secretory autophagy during bacterial infection of the intestine. *Science (New York, N.Y.)*, *357*(6355), 1047–1052. https://doi.org/10.1126/science.aal4677

Berish, R. B., Ali, A. N., Telmer, P. G., Ronald, J. A., & Leong, H. S. (2018). Translational models of prostate cancer bone metastasis. *Nature Reviews. Urology*, *15*(7), 403–421. https://doi.org/10.1038/s41585-018-0020-2

Cadwell, K., & Debnath, J. (2018). Beyond self-eating: The control of nonautophagic functions and signaling pathways by autophagy-related proteins. *The Journal of Cell Biology*, *217*(3), 813–822. https://doi.org/10.1083/jcb.201706157

Croucher, P. I., McDonald, M. M., & Martin, T. J. (2016). Bone metastasis: The importance of the neighbourhood. *Nature Reviews. Cancer*, *16*(6), 373–386. https://doi.org/10.1038/nrc.2016.44

DeSelm, C. J., Miller, B. C., Zou, W., Beatty, W. L., van Meel, E., Takahata, Y., Klumperman, J., Tooze, S. A., Teitelbaum, S. L., & Virgin, H. W. (2011). Autophagy proteins regulate the secretory component of osteoclastic bone resorption. *Developmental Cell*, *21*(5), 966–974. https://doi.org/10.1016/j.devcel.2011.08.016

Dupont, N., Jiang, S., Pilli, M., Ornatowski, W., Bhattacharya, D., & Deretic, V. (2011). Autophagy-based unconventional secretory pathway for extracellular delivery of IL-1β. *The EMBO Journal*, *30*(23), 4701–4711. https://doi.org/10.1038/emboj.2011.398

Eden, E. R., White, I. J., Tsapara, A., & Futter, C. E. (2010). Membrane contacts between endosomes and ER provide sites for PTP1B-epidermal growth factor receptor interaction. *Nature Cell Biology*, *12*(3), 267–272. https://doi.org/10.1038/ncb2026

Feng, Z., Hensley, L., McKnight, K. L., Hu, F., Madden, V., Ping, L., Jeong, S. H., Walker, C., Lanford, R. E., & Lemon, S. M. (2013). A pathogenic picornavirus acquires an envelope by hijacking cellular membranes. *Nature*, *496*(7445), 367–371. https://doi.org/10.1038/nature12029

Feng, Z., Li, Y., McKnight, K. L., Hensley, L., Lanford, R. E., Walker, C. M., & Lemon, S. M. (2015). Human pDCs preferentially sense enveloped hepatitis A virions. *The Journal of Clinical Investigation*, *125*(1), 169–176. https://doi.org/10.1172/JCI77527

Glass, D. A., 2nd, Bialek, P., Ahn, J. D., Starbuck, M., Patel, M. S., Clevers, H., Taketo, M. M., Long, F., McMahon, A. P., Lang, R. A., & Karsenty, G. (2005). Canonical Wnt signaling in differentiated osteoblasts controls osteoclast differentiation. *Developmental Cell*, *8*(5), 751–764. https://doi.org/10.1016/j.devcel.2005.02.017

Grein van der, S. G., Defourny, K. A. Y., Rabouw, H. H., Goerdayal, S. S., Herwijnen van, M. J. C., Wubbolts, R. W., Altelaar, M., van Kuppeveld, F. J. M., & Nolte-'t Hoen, E. N. M. (2022). The encephalomyocarditis virus Leader promotes the release of virions inside extracellular vesicles via the induction of secretory autophagy. *Nature Communications*, *13*(1), 3625. https://doi.org/10.1038/s41467-022-31181-y

Itakura, E., Kishi-Itakura, C., & Mizushima, N. (2012). The hairpin-type tail-anchored SNARE syntaxin 17 targets to autophagosomes for fusion with endosomes/lysosomes. *Cell*, *151*(6), 1256–1269. https://doi.org/10.1016/j.cell.2012.11.001

Jumper, J., Evans, R., Pritzel, A., Green, T., Figurnov, M., Ronneberger, O., Tunyasuvunakool, K., Bates, R., Žídek, A., Potapenko, A., Bridgland, A., Meyer, C., Kohl, S. A. A., Ballard, A. J., Cowie, A., Romera-Paredes, B., Nikolov, S., Jain, R., Adler, J., … Hassabis, D. (2021). Highly accurate protein structure prediction with AlphaFold. *Nature*, *596*(7873), 583–589. https://doi.org/10.1038/s41586-021-03819-2

Kalluri, R., & LeBleu, V. S. (2020). The biology, function, and biomedical applications of exosomes. *Science (New York, N.Y.)*, *367*(6478), eaau6977. https://doi.org/10.1126/science.aau6977

Keller, M. D., Ching, K. L., Liang, F. X., Dhabaria, A., Tam, K., Ueberheide, B. M., Unutmaz, D., Torres, V. J., & Cadwell, K. (2020). Decoy exosomes provide protection against bacterial toxins. *Nature*, *579*(7798), 260–264. https://doi.org/10.1038/s41586-020-2066-6

Kim, B., Kim, H., Jung, S., Moon, A., Noh, D. Y., Lee, Z. H., Kim, H. J., & Kim, H. H. (2020). A CTGF-RUNX2-RANKL axis in breast and prostate cancer cells promotes tumor progression in bone. *Journal of Bone and Mineral Research*, *35*(1), 155–166. https://doi.org/10.1002/jbmr.3869

Kimura, T., Jia, J., Kumar, S., Choi, S. W., Gu, Y., Mudd, M., Dupont, N., Jiang, S., Peters, R., Farzam, F., Jain, A., Lidke, K. A., Adams, C. M., Johansen, T., & Deretic, V. (2017). Dedicated SNAREs and specialized TRIM cargo receptors mediate secretory autophagy. *The EMBO Journal*, *36*(1), 42–60. https://doi.org/10.15252/embj.201695081

Leidal, A. M., Huang, H. H., Marsh, T., Solvik, T., Zhang, D., Ye, J., Kai, F., Goldsmith, J., Liu, J. Y., Huang, Y. H., Monkkonen, T., Vlahakis, A., Huang, E. J., Goodarzi, H., Yu, L., Wiita, A. P., & Debnath, J. (2020). The LC3-conjugation machinery specifies the loading of RNA-binding proteins into extracellular vesicles. *Nature Cell Biology*, *22*(2), 187–199. https://doi.org/10.1038/s41556-019-0450-y

Li, M. Y., Naik, T. S., Siu, L. Y. L., Acuto, O., Spooner, E., Wang, P., Yang, X., Lin, Y., Bruzzone, R., Ashour, J., Evans, M. J., & Sanyal, S. (2020). Lyn kinase regulates egress of flaviviruses in autophagosome-derived organelles. *Nature Communications*, *11*(1), 5189. https://doi.org/10.1038/s41467-020-19028-w

Ma, Q., Liang, M., Wu, Y., Dou, C., Xu, J., Dong, S., & Luo, F. (2021). Small extracellular vesicles deliver osteolytic effectors and mediate cancer-induced osteolysis in bone metastatic niche. *Journal of Extracellular Vesicles*, *10*(4), e12068. https://doi.org/10.1002/jev2.12068

Malhotra, V. (2013). Unconventional protein secretion: An evolving mechanism. *The EMBO Journal*, *32*(12), 1660–1664. https://doi.org/10.1038/emboj.2013.104

Matsui, T., Jiang, P., Nakano, S., Sakamaki, Y., Yamamoto, H., & Mizushima, N. (2018). Autophagosomal YKT6 is required for fusion with lysosomes independently of syntaxin 17. *The Journal of Cell Biology*, *217*(8), 2633–2645. https://doi.org/10.1083/jcb.201712058

Mauvezin, C., Nagy, P., Juhász, G., & Neufeld, T. P. (2015). Autophagosome-lysosome fusion is independent of V-ATPase-mediated acidification. *Nature Communications*, *6*, 7007. https://doi.org/10.1038/ncomms8007

Mauvezin, C., & Neufeld, T. P. (2015). Bafilomycin A1 disrupts autophagic flux by inhibiting both V-ATPase-dependent acidification and Ca-P60A/SERCA-dependent autophagosome-lysosome fusion. *Autophagy*, *11*(8), 1437–1438. https://doi.org/10.1080/15548627.2015.1066957

Nagashima, S., Takahashi, M., Kobayashi, T., Tanggis, Nishizawa, T., Nishiyama, T., Primadharsini, P. P., & Okamoto, H. (2017). Characterization of the quasi-enveloped hepatitis E virus particles released by the cellular exosomal pathway. *Journal of Virology*, *91*(22), e00822–e00817. https://doi.org/10.1128/JVI.00822-17

Nakatogawa, H. (2020). Mechanisms governing autophagosome biogenesis. *Nature Reviews. Molecular cell biology*, *21*(8), 439–458. https://doi.org/10.1038/s41580-020-0241-0

Nguyen, D. X., Bos, P. D., & Massagué, J. (2009). Metastasis: From dissemination to organ-specific colonization. *Nature Reviews. Cancer*, *9*(4), 274–284. https://doi.org/10.1038/nrc2622

Ostrowski, M., Carmo, N. B., Krumeich, S., Fanget, I., Raposo, G., Savina, A., Moita, C. F., Schauer, K., Hume, A. N., Freitas, R. P., Goud, B., Benaroch, P., Hacohen, N., Fukuda, M., Desnos, C., Seabra, M. C., Darchen, F., Amigorena, S., Moita, L. F., & Thery, C. (2010). Rab27a and Rab27b control different steps of the exosome secretion pathway. *Nature Cell Biology*, *12*(1), 19–13. https://doi.org/10.1038/ncb2000

Rohde, M., & Mayer, H. (2007). Exocytotic process as a novel model for mineralization by osteoblasts in vitro and in vivo determined by electron microscopic analysis. *Calcified Tissue International*, *80*(5), 323–336. https://doi.org/10.1007/s00223-007-9013-5

Solvik, T. A., Nguyen, T. A., Tony Lin, Y. H., Marsh, T., Huang, E. J., Wiita, A. P., Debnath, J., & Leidal, A. M. (2022). Secretory autophagy maintains proteostasis upon lysosome inhibition. *The Journal of Cell Biology*, *221*(6), e202110151. https://doi.org/10.1083/jcb.202110151

Sturge, J., Caley, M. P., & Waxman, J. (2011). Bone metastasis in prostate cancer: Emerging therapeutic strategies. *Nature Reviews. Clinical Oncology*, *8*(6), 357–368. https://doi.org/10.1038/nrclinonc.2011.67

Vrahnas, C., Blank, M., Dite, T. A., Tatarczuch, L., Ansari, N., Crimeen-Irwin, B., Nguyen, H., Forwood, M. R., Hu, Y., Ikegame, M., Bambery, K. R., Petibois, C., Mackie, E. J., Tobin, M. J., Smyth, G. K., Oakhill, J. S., Martin, T. J., & Sims, N. A. (2019). Increased autophagy in EphrinB2-deficient osteocytes is associated with elevated secondary mineralization and brittle bone. *Nature Communications*, *10*(1), 3436. https://doi.org/10.1038/s41467-019-11373-9

Wang, G., Li, J., Bojmar, L., Chen, H., Li, Z., Tobias, G. C., Hu, M., Homan, E. A., Lucotti, S., Zhao, F., Posada, V., Oxley, P. R., Cioffi, M., Kim, H. S., Wang, H., Lauritzen, P., Boudreau, N., Shi, Z., Burd, C. E., … Lyden, D. (2023). Tumour extracellular vesicles and particles induce liver metabolic dysfunction. *Nature*, *618*(7964), 374–382. https://doi.org/10.1038/s41586-023-06114-4

Wang, Z. X., Luo, Z. W., Li, F. X., Cao, J., Rao, S. S., Liu, Y. W., Wang, Y. Y., Zhu, G. Q., Gong, J. S., Zou, J. T., Wang, Q., Tan, Y. J., Zhang, Y., Hu, Y., Li, Y. Y., Yin, H., Wang, X. K., He, Z. H., Ren, L., … Xie, H. (2022). Aged bone matrix-derived extracellular vesicles as a messenger for calcification paradox. *Nature Communications*, *13*(1), 1453. https://doi.org/10.1038/s41467-022-29191-x

Yan, J., Shen, M., Sui, B., Lu, W., Han, X., Wan, Q., Liu, Y., Kang, J., Qin, W., Zhang, Z., Chen, D., Cao, Y., Ying, S., Tay, F. R., Niu, L. N., & Jiao, K. (2022). Autophagic LC3^{+} calcified extracellular vesicles initiate cartilage calcification in osteoarthritis. *Science Advances*, *8*(19), eabn1556. https://doi.org/10.1126/sciadv.abn1556

Yoshida, G., Kawabata, T., Takamatsu, H., Saita, S., Nakamura, S., Nishikawa, K., Fujiwara, M., Enokidani, Y., Yamamuro, T., Tabata, K., Hamasaki, M., Ishii, M., Kumanogoh, A., & Yoshimori, T. (2022). Degradation of the NOTCH intracellular domain by elevated autophagy in osteoblasts promotes osteoblast differentiation and alleviates osteoporosis. *Autophagy*, *18*(10), 2323–2332. https://doi.org/10.1080/15548627.2021.2017587

SUPPORTING INFORMATION

Additional supporting information can be found online in the Supporting Information section at the end of this article.

How to cite this article: Wei, X., Liang, M., Deng, M., Zheng, J., Luo, F., & Ma, Q. (2024). A switch from lysosomal degradation to secretory autophagy initiates osteogenic bone metastasis in prostate cancer. *Journal of Extracellular Vesicles*, *13*, e70002. https://doi.org/10.1002/jev2.70002